Numer. Math. (1998) 78: 619–658

Numerische Mathematik

Electronic Edition

A dual graph-norm refinement indicator for finite volume approximations of the Euler equations

Thomas Sonar[1], **Endre Süli**[2]

[1] Institut für Angewandte Mathematik, Universität Hamburg, Bundesstraße 55, D-20146 Hamburg, Germany; e-mail: Thomas.Sonar@math.uni-hamburg.de
[2] Oxford University Computing Laboratory, Wolfson Building, Parks Road, Oxford OX1 3OD, UK; e-mail: Endre.Suli@comlab.oxford.ac.uk

Received May 15, 1995 / Revised version received April 17, 1996

Summary. We generalise and apply a refinement indicator of the type originally designed by Mackenzie, Süli and Warnecke in [15] and [16] for linear Friedrichs systems to the Euler equations of inviscid, compressible fluid flow. The Euler equations are symmetrized by means of entropy variables and locally linearized about a constant state to obtain a symmetric hyperbolic system to which an *a posteriori* error analysis of the type introduced in [15] can be applied. We discuss the details of the implementation of the refinement indicator into the DLR-τ-Code which is based on a finite volume method of box type on an unstructured grid and present numerical results.

Mathematics Subject Classification (1991): 65M20, 65M50, 65M60; 76M99

1 Introduction

Adaptive a posteriori error control is now a well-established device in the finite element solution of elliptic and parabolic problems. Unfortunately, there is a lack of an analogous theoretical framework for finite volume approximations of hyperbolic equations in gas dynamics. The absence of such an analysis can be attributed to the inherent nonlinearity of the equations, the incompleteness of the corresponding well-posedness theory, as well as to the fact that the basic stability and accuracy properties of finite volume methods for this class of partial differential equations are not well understood. Inspired by results of C. Johnson et al. [7] concerning error indicators for the streamline diffusion finite element method, in [21] we introduced weighted residual-based refinement indicators for finite volume approximations of the equations of compressible fluid flow. We begin with an informal outline of this approach.

Correspondence to: T. Sonar

Consider the partial differential equation

$$\mathscr{L}u = f$$

on a given domain $\Omega \subset \mathbb{R}^N$, where $\mathscr{L}$ denotes an invertible linear differential operator of first order possessing a bounded inverse operator $\mathscr{L}^{-1}$. Denoting by u^h the finite volume approximation to the analytical solution u, we define the global error of the method as

$$e^h := u^h - u. \tag{1.1}$$

Letting

$$r^h := \mathscr{L}u^h - f \tag{1.2}$$

be the corresponding residual, it follows that

$$r^h = \mathscr{L}e^h.$$

Hence

$$\|e^h\|_{(1)} \leq |||\mathscr{L}^{-1}|||\, \|r^h\|_{(2)}, \tag{1.3}$$

with suitable norms $\|\cdot\|_{(1)}$, $\|\cdot\|_{(2)}$ and $|||\cdot|||$. In contrast with the global error e, the residual is a computable quantity even if the true solution is not known. Assuming that an upper bound on $|||\mathscr{L}^{-1}|||$ is available, inequality (1.3) can be used for reliable a posteriori error estimation and adaptive error control. Of course, it may happen that the error is very much overestimated by the right-hand side of (1.3) so that unnecessarily fine grids are generated, which in turn degrades the efficiency of the underlying adaptive method. However, if in addition to (1.3) an inequality of the form

$$c\|r^h\|_{(2)} \leq \|e^h\|_{(1)}$$

is available, where c is a computable constant, then the efficiency of the adaptive numerical method can be ensured.

If $\mathscr{L}$ is nonlinear and most of its properties are unknown, it is unlikely that a relation of the form

$$c_1\|r^h\|_{(2)} \leq \|e^h\|_{(1)} \leq c_2\|r^h\|_{(2)} \tag{1.4}$$

will be available with computable constants c_1 and c_2; indeed, for the Euler equations of compressible multi-dimensional gas dynamics it is practically impossible to determine the norms $\|\cdot\|_{(1)}$ and $\|\cdot\|_{(2)}$ and the constants c_1 and c_2.

Thus, in [21], the L^2-norm of the residual was examined as an ad hoc error indicator for finite volume approximations of compressible flow problems. It was shown, by means of a simple one-dimensional example, that, in the presence of a discontinuous solution, $\|r^h\|_{L^2(\Omega)} \to \infty$ as $h \to 0$. More generally, if u^h is an approximation to a discontinuous solution u in $\Omega \subset \mathbb{R}^N$, then

$$\|r^h\|_{L^2(\Omega)} = \mathscr{O}\left(h^{-\frac{1}{2}}\right),$$

see [22]. To remedy the situation, in [21], the scaled refinement indicator

$$R^h_{L^2} := h\|r^h\|_{L^2(T)}$$

was used on each triangle T of a triangulation $\mathscr{T}^h \subset \mathbb{R}^2$. Here, h is a local measure of T, such as the length of the longest edge. Besides the desire to counteract the $\mathscr{O}(1/\sqrt{h})$ behaviour of the L^2-norm of the residual, the choice of the exponent of h in the definition of $R^h_{L^2}$ was motivated by the form of typical residual-based a posteriori error bounds for the streamline diffusion method, see [21]. There the power of h occurs naturally in the numerical treatment of hyperbolic model problems due to the properties of the method and, in particular, to the presence of numerical dissipation. Unfortunately, there is no analogous theory for finite volume approximations of hyperbolic problems.

Another ad hoc indicator considered by the authors (see [21]) is

$$R^h_{H^{-1}} := \|r^h\|_{H^{-1}(T)}.$$

This was motivated by the observation that if the analytical solution u of $\mathscr{L}u = f$ is discontinuous and u^h converges to u in $L^2(\Omega)$, then, at least for a linear differential operator $\mathscr{L}$, the residual $r^h = \mathscr{L}u^h - f$ converges to zero in $H^{-1}(\Omega)$. The H^{-1} refinement indicator, although not computable, was approximated using a local subdivision technique in [21]; this lead to results which were very comparable to those obtained with the $R^h_{L^2}$-indicator. Although a posteriori error estimation by these ad hoc error indicators is possible and the computations based on them yield satisfactory results, it is unlikely for first-order hyperbolic systems that they satisfy two-sided error bounds of the form (1.4), with $\|\cdot\|_{(1)} = \|\cdot\|_{L^2(\Omega)}$. Consequently, there is no guarantee that they provide reliable or efficient estimates of the error in the L^2-norm. The aim of this paper is to pursue a mathematically systematic approach to arrive at a two-sided a posteriori bound of the form (1.4) for the error in the L^2-norm.

Our work here is a development of the techniques introduced by Mackenzie, Süli and Warnecke in [15], where two-sided a posteriori error bounds were derived for Petrov-Galerkin finite element approximations of Friedrichs systems. There, the approach was based on a decomposition of the global error of the numerical method into a locally created part e^{cell} whose properties are entirely governed by the local cell residual, and a propagating component e^{trans} which is transported into the cell through the inflow boundary. It was shown in [15] that

$$\|r^h\|_{D'(\mathscr{L}^*,T)} \le \|e^{\text{cell}}\|_{L^2(T)} \le \frac{1}{c}\|r^h\|_{D'(\mathscr{L}^*,T)}$$

holds on each computational cell T, where $\|\cdot\|_{D'(\mathscr{L}^*,T)}$ is the, so called, dual graph-norm and $\mathscr{L}^*$ the formal adjoint operator of $\mathscr{L}$. The viability of residual-based local a posteriori error estimation hinges on the assumption that the cell error dominates the transported error.

In this paper, following a similar approach, we perform an a posteriori error analysis for finite volume approximations of the compressible Euler equations of gas dynamics, exploiting a symmetrisation by means of entropy variables followed by local linearisation about a constant mean state. The resulting system

is of Friedrichs type and thus an a posteriori error analysis analogous to the one developed in [15] is possible. Since the symmetrised Euler equations are rarely used in practice we perform the computation of the approximate solution u^h in the conserved physical variables. The dual graph-norm indicator can then be computed element-by-element from u^h by means of a carefully chosen approximation procedure. To the best of our knowledge, this is the first refinement indicator for finite volume approximations of Euler's equations which is – in the sense of local linearisation – with a sound mathematical foundation.

2 Symmetrisation of the Euler equations

2.1 The Euler equations

We consider plane flow of an inviscid, compressible, ideal gas. Denoting by $\rho, v = (v_1, v_2), p, E$ the density, cartesian velocity, pressure and total energy, respectively, the equations of motion are

$$\partial_t u + \sum_{i=1}^{2} \partial_{x_i} f_i(u) = 0, \tag{2.1}$$

where the vector of conservative variables u and the fluxes $f_i(u)$ are defined by

$$u := \begin{bmatrix} \rho \\ \rho v_1 \\ \rho v_2 \\ \rho E \end{bmatrix}, \quad f_i(u) := \begin{bmatrix} \rho v_i \\ \rho v_1 v_i + p\delta_1^i \\ \rho v_2 v_i + p\delta_2^i \\ \rho H v_i \end{bmatrix}.$$

The quantity δ_k^i denotes the Kronecker-delta while H is the total enthalpy defined as

$$H = E + \frac{p}{\rho}.$$

The range of the conservative variables is a subset S of $\mathbb{R}^4$ called the state space. The equation of state for an ideal gas is given by

$$p = (\kappa - 1)\rho \left(E - \frac{|v|^2}{2} \right)$$

where κ is the ratio of specific heats which, for dry air, is $\kappa = 1.405$.

If the flow is sufficiently smooth, (2.1) can be equivalently expressed in quasilinear (non-conservative) form as

$$\partial_t u + \sum_{i=1}^{2} A_i(u) \partial_{x_i} u = 0 \tag{2.2}$$

where the $A_i(u) := \nabla_u f_i(u)$ denote the Jacobian matrices of the fluxes, given by

$$A_1(u) = \begin{bmatrix} 0 & 1 & 0 & 1 \\ \frac{\kappa-3}{2}v_1^2 + \frac{\kappa-1}{2}v_2^2 & (3-\kappa)v_1 & (1-\kappa)v_2 & \kappa - 1 \\ -v_1 v_2 & v_2 & v_1 & 0 \\ (\kappa-1)v_1|v|^2 - \kappa v_1 E & \kappa E - \frac{\kappa-1}{2}(v_2^2 + 3v_1^2) & (1-\kappa)v_1 v_2 & \kappa v_1 \end{bmatrix}$$

$$A_2(u) = \begin{bmatrix} 0 & 0 & 1 & 0 \\ -v_1 v_2 & v_2 & v_1 & 0 \\ \frac{\kappa-3}{2}v_2^2 + \frac{\kappa-1}{2}v_1^2 & (1-\kappa)v_1 & (3-\kappa)v_2 & \kappa - 1 \\ (\kappa-1)v_2|v|^2 - \kappa v_2 E & (1-\kappa)v_1 v_2 & \kappa E - \frac{\kappa-1}{2}(v_1^2 + 3v_2^2) & \kappa v_2 \end{bmatrix}.$$

The system (2.1) of Euler's equations is hyperbolic, i.e. the matrix

$$A(u, \nu) := \sum_{i=1}^{2} \nu_i A_i(u)$$

possesses four real eigenvalues $\lambda_i(u, \nu), i = 1, \ldots, 4$, for all values of $u \in S$ and all $\nu \in \mathbb{R}^2$. Although the matrices $A_i, i = 1, 2$, can be individually diagonalised, it is well known that they cannot be diagonalised simultaneously. To see this, note that the product of the Jacobian matrices is not symmetric, i.e.

$$(A_1(u)A_2(u))^* \neq A_1(u)A_2(u).$$

Note that the adjoint matrix in the case of Euler's equations is simply the transpose. If both Jacobian matrices could be diagonalised simultaneously there would exist an orthogonal transformation matrix $D(u) \in \mathbb{R}^{4\times 4}$ such that

$$D^{-1}(u)A_i(u)D(u) = \Lambda_i(u), \quad i = 1, 2,$$

where $\Lambda(u)$ is the required diagonal matrix. If we assume the existence of such a matrix the calculation

$$\begin{aligned} D^{-1}(u)A_1(u)A_2(u)D(u) &= D^{-1}(u)A_1(u)D(u)D^{-1}(u)A_2(u)D(u) \\ &= \Lambda_1(u)\Lambda_2(u) \\ &=: \Lambda_3(u) = \Lambda_3^*(u) = \left(D^{-1}(u)A_1(u)A_2(u)D(u)\right)^* \\ &= D^{-1}(u)(A_1(u)A_2(u))^*D(u) \end{aligned}$$

shows that the product $A_1(u)A_2(u)$ is then necessarily symmetric, which leads to a contradiction.

Nevertheless, Euler's equations can be symmetrised by exploiting the entropy variables. The precise description of this symmetrisation is the subject of the next section.

2.2 Entropy variables

We assume that an entropy inequality holds for all weak solutions of Euler's equations, i.e. for functions $u \in BV([0,t^*];L^1 \cap L^\infty(\Omega)), t^* > 0$, such that

$$\frac{d}{dt}\int_\sigma u\,dx = -\oint_{\partial\sigma}\sum_{i=1}^{2} f_i(u)\hat{\nu}_i\,ds$$

holds on every *control volume* $\sigma \subset \mathbb{R}^2$. For our purposes a control volume is a bounded simply connected domain with polygonal boundary and outer unit vector $\hat{\nu} = (\hat{\nu}_1, \hat{\nu}_2)$, defined almost everywhere on $\partial\sigma$. Thus we assume the existence of an entropy function

$$S \ni u \overset{\eta}{\longmapsto} \eta(u) \in \mathbb{R}$$

as well as the existence of entropy fluxes

$$S \ni u \overset{q_i}{\longmapsto} q_i \in \mathbb{R}$$

which are compatible with η in the sense that

$$\nabla_u \eta(u) \cdot A_i(u) = \nabla_u q_i(u); \quad i = 1,2.$$

The entropy and the entropy fluxes are, furthermore, assumed to satisfy an entropy inequality

$$\partial_t \eta(u) + \sum_{i=1}^{2} \partial_{x_i} q_i(u) \le 0$$

in the weak sense, i.e.

$$\frac{d}{dt}\int_\sigma \eta(u)\,dx \le -\oint_{\partial\sigma}\sum_{i=1}^{2} q_i(u)\hat{\nu}_i\,ds$$

holds on each control volume σ. Note that the entropy inequality is the mathematical model of the second law of thermodynamics. In the case of Euler's equations the thermodynamical entropy density

$$\eta(u) := -\rho s$$

with entropy

$$s := \log\frac{p}{\rho^\kappa}$$

is a candidate for an entropy function. The discrepancy in the signs of the two entropies is due to the historical convention that a mathematical entropy is convex, by definition, while the thermodynamical entropy is defined to be a concave function.

We convert the Euler equations (2.1) into a symmetric system of partial differential equations using an invertible change of variables

$$u \longmapsto U(u).$$

The following theorem, due to Mock (see [8], [18]), identifies the role of the entropy.

Theorem 2.1. *If η is an entropy function then the change of variables*

$$S \ni u \overset{U}{\longmapsto} U(u) := \nabla_u \eta(u)$$

symmetrises the system (2.1).

Applying this change of variables to system (2.1), we obtain the system of partial differential equations

$$\partial_t u(U) + \sum_{i=1}^{2} \partial_{x_i} f_i(u(U)) = 0 \tag{2.3}$$

which is still in conservation form. Writing $F_i(U) := f_i(u(U))$, and using the chain rule, yields

$$(\nabla_U u)\, \partial_t U + \sum_{i=1}^{2} (\nabla_u f_i(u(U)))\, (\nabla_U u)\, \partial_{x_i} U = 0,$$

or, denoting $A^0(U) := \nabla_U u$, we can write this as

$$A^0(U)\partial_t U + \sum_{i=1}^{2} A_i(u(U)) A^0(U) \partial_{x_i} U = 0. \tag{2.4}$$

The mapping $u \longmapsto U$ is given by

$$U(u) = \frac{\kappa - 1}{p} \begin{bmatrix} \frac{p}{\kappa-1}(\kappa + 1 - s) - \rho E \\ \rho v_1 \\ \rho v_2 \\ -\rho \end{bmatrix} =: \begin{bmatrix} U_1 \\ U_2 \\ U_3 \\ U_4 \end{bmatrix}, \tag{2.5}$$

while the inverse $U \longmapsto u$ is given by

$$u(U) = \frac{p}{\kappa - 1} \begin{bmatrix} -U_4 \\ U_2 \\ U_3 \\ 1 - \frac{1}{2}\frac{U_2^2 + U_3^2}{U_4} \end{bmatrix},$$

see [13], for example. Thus,

$$A^0 = \frac{1}{\kappa - 1} \begin{bmatrix} \rho & \rho v_1 & \rho v_2 & \frac{p}{\kappa-1} + \frac{1}{2}\rho|v|^2 \\ & p + \rho v_1^2 & \rho v_1 v_2 & \frac{1}{2}\rho v_1 |v|^2 + \frac{\kappa v_1 p}{\kappa-1} \\ & & p + \rho v_2^2 & \frac{1}{2}\rho v_2 |v|^2 + \frac{\kappa v_2 p}{\kappa-1} \\ \text{symm} & & & \frac{1}{4}\rho|v|^2 - \frac{\kappa |v|^2 p^2}{(\kappa-1)^2} + \frac{\kappa p^2}{\rho(\kappa-1)^2} \end{bmatrix},$$

while its inverse $A^{0^{-1}}$ is given by

$$A^{0^{-1}} = \frac{\kappa - 1}{p^2} \begin{bmatrix} \frac{1}{4}\rho|v|^2 + \frac{\kappa p^2}{\kappa - 1} & \frac{1}{2}\rho v_1|v|^2 & \frac{1}{2}\rho v_2|v|^2 & \frac{p}{\kappa-1} - \frac{1}{2}\rho|v|^2 \\ & \rho v_1^2 + \frac{p}{\kappa-1} & \rho v_1 v_2 & -\rho v_1 \\ & & \rho v_2^2 + \frac{p}{\kappa-1} & -\rho v_2 \\ \text{symm} & & & \rho \end{bmatrix}.$$

Thus, we can rewrite the system as

$$\sum_{i=0}^{2} M_i(U)\partial_{x_i} U = 0,$$

where $M_0(U) := A^0(U)$ and $M_i(U) := A_i(u(U))A^0(U), i = 1, 2$, are symmetric 4×4 matrices and $x_0 := t$. The symmetry of the matrices M_i can be shown by evaluating the matrix product. A direct proof can be given along the following lines. Define functions $\mathbf{r}(U) := U^* u(U) - \eta(u(U))$ and $\mathbf{s}_i(U) := U^* f_i(u(U)) - q_i(u(U)), i = 1, 2$. Since the compatibility relation $\nabla_u \eta(u) = A_i(u) q_i(u)$ between entropy and entropy fluxes changes under the transformation of variables to $U^* \nabla_U f_i(u(U)) = \nabla_U q_i(u(U))$ the derivatives of $\mathbf{r}$ and $\mathbf{s}$ are given by

$$\begin{aligned} \nabla_U \mathsf{r}(U) &= u(U) \\ \nabla_U \mathsf{s}_i(U) &= f_i(u(U)), \quad i = 1, 2. \end{aligned}$$

Taking derivatives again shows that

$$\begin{aligned} \nabla_U^2 \mathsf{r}(U) &= \nabla_U u(U) \\ \nabla_U^2 \mathsf{s}_i(U) &= \nabla_U f_i(u(U)), \quad i = 1, 2. \end{aligned}$$

This indicates that the Jacobian matrices of the transformed fluxes are the Hessians of the auxiliary functions s_i and hence symmetric.

Applying $A^{0^{-1}}$ to (2.4) from the left, we arrive at the system

$$\partial_t U + \sum_{i=1}^{2} A^{0^{-1}}(U) A_i(u(U)) A^0(U)\, \partial_{x_i} U = 0.$$

We can rewrite this as

$$\sum_{i=0}^{2} \tilde{M}_i(U)\partial_{x_i} U = 0 \tag{2.6}$$

where the $\tilde{M}_i$ are non-symmetric 4×4 matrices given by

$$\begin{aligned} \tilde{M}_0(U) &:= I, \\ \tilde{M}_i(U) &:= A^{0^{-1}}(U) M_i(U), \quad i = 1, 2. \end{aligned}$$

Equivalently, if we define the matrix

$$A_0 := I,$$

all $\tilde{M}_i$ are given by $\tilde{M}_i(U) := A^{0^{-1}}(U) A_i(u(U)) A^0(U)$ for $i = 0, 1, 2$.

Next, we perform a local linearisation of (2.4) about a mean constant state in each cell, thus obtaining a linear symmetric positive (Friedrichs) system in the entropy variables for which an a posteriori error analysis, similar to the one proposed in [15], may be carried out.

2.3 Local linearisation

We consider the non-linear system (2.3) and assume the existence of a mean constant state $U_c \in \mathbb{R}^4$ such that the decomposition

$$U = U_c + V$$

holds for a small non-constant perturbation function V. It follows that

$$\begin{aligned} u(U) &= u(U_c + V) = u(U_c) + \nabla_U u(U_c)V + \mathcal{O}(|V|^2) \\ &= u(U_c) + A^0(U_c)V + \mathcal{O}(|V|^2) \end{aligned}$$

and

$$\begin{aligned} f_i(u(U)) &\equiv F_i(U) = F_i(U_c + V) = F_i(U_c) + \nabla_U F_i(U_c)V + \mathcal{O}(|V|^2) \\ &= F_i(U_c) + \nabla_U f_i(u(U_c))V + \mathcal{O}(|V|^2) \\ &= F_i(U_c) + \nabla_u f_i(u(U_c))(\nabla_U u)V + \mathcal{O}(|V|^2) \\ &= F_i(U_c) + A_i(u(U_c))A^0(U_c)V + \mathcal{O}(|V|^2). \end{aligned}$$

Writing $u_c := u(U_c)$ and dropping the $\mathcal{O}(|V|^2)$ terms, we get the symmetric system

$$A^0(U_c)\partial_t V + \sum_{i=1}^{2} A_i(u_c)A^0(U_c)\partial_{x_i} V = 0, \tag{2.7}$$

where all matrix elements are constant. Applying the inverse constant matrix $A^{0^{-1}}(U_c)$ from the left yields the non-symmetric linear system

$$\partial_t V + \sum_{i=1}^{2} A^{0^{-1}}(U_c)A_i(u_c)A^0(U_c)\partial_{x_i} V = 0. \tag{2.8}$$

Equation (2.7) is our starting point for the a posteriori error analysis; it can be rewritten as

$$\mathcal{L}V := \sum_{i=0}^{2} M_i(U_c)\partial_{x_i} V = 0, \tag{2.9}$$

where the M_i are evaluated at the constant state U_c, i.e.

$$\begin{aligned} M_0(U_c) &:= A^0(U_c), \\ M_i(U_c) &:= A_i(u_c)A^0(U_c), \quad i = 1, 2. \end{aligned}$$

If only steady flow problems are considered then $\partial_t V \equiv 0$ and the system (2.7) collapses to

$$\sum_{i=1}^{2} A_i(u_c)A^0(U_c)\partial_{x_i} V = 0.$$

Note that in contrast with the variable-coefficient operators studied in [15], here the operator $\mathcal{L}$ has constant coefficients.

3 Primary and secondary grids

We consider compressible fluid flow in a bounded domain $\Omega \subset \mathbb{R}^2$; for the sake of simplicity, Ω is assumed to have a polygonal boundary $\partial\Omega$. On $\overline{\Omega}$ we define a triangulation $\mathscr{T}^h$ as a partition of $\overline{\Omega}$ into finitely many subsets $T_i \subset \overline{\Omega}$, $i = 1, \ldots, \#T$, such that:

- $\overline{\Omega} = \cup_{i \in \{1,\ldots,\#T\}} T_i$;
- Every $T_i \subset \mathscr{T}^h$ is closed with non-empty interior;
- For any two $T_i, T_j \in \mathscr{T}^h$, with $i \neq j$, the interiors of T_i and T_j are disjoint;
- Each $T_i \in \mathscr{T}^h$ has polygonial boundary.

We use a conforming triangulation of Ω, in the sense that every edge of each $T_i \in \mathscr{T}^h$ is either a subset of the boundary $\partial\Omega := \overline{\Omega}\backslash\Omega$ or the edge of another $T_j \in \mathscr{T}^h$ with $i \neq j$.

For the finite volume method considered here the actual shape of T_i is of no significance; however, for the sake of computational simplicity, we use triangular elements. The conforming triangulation of Ω is called the *primary grid*.
In addition to the primary grid we consider what we call the *secondary grid*, see [12]. This is defined as follows. Let

$$K_{h,i} := \{T \in \mathscr{T}^h \mid \text{ node } i \text{ is a vertex of } T\}$$

be the set of all triangles surrounding node i, and $e_{T,k}, k = 1, 2, 3$, the three edges of triangle T. Then

$$E_{h,i} := \{e_{T,k} \mid T \in \mathscr{T}^h, k \in \{1, 2, 3\}, \text{ node } i \text{ is a vertex of } e_{T,k}\}$$

is the set of all edges emanating from point i. The subset $B_i \subset \overline{\Omega}$ defined as the region surrounding node i, bounded by the straight line segments joining the barycentres of $T_k \in K_{h,i}$ with the midpoints of the edges $e_{T_k,j}$, is called a box or control volume. If i is a node on $\partial\Omega$ then box B_i is defined as the region around node i, bounded by the straight line segments joining the barycentres of $T_k \in K_{h,i}$ with the midpoints of the edges $e_{T_k,j}$, and joining the midpoints of the edges of $e_{T_k,j}$ that lie on $\partial\Omega$ to node i. Various configurations of primary and secondary grids are shown in Figs. 1 and 2. The DLR-τ-Code is based on a finite volume discretisation using discontinuous piecewise polynomial functions to approximate the analytical solution on the boxes; restricting these to the vertices of the triangles in the primary grid one can construct a continuous piecewise linear interpolant over the triangulation $\mathscr{T}^h$ which can be considered as an approximation of the analytical solution on the primary grid. It is this latter approximation that will be exploited in the calculation of the local error indicators. The actual definition of the finite volume approximation u^h to the analytical solution u is irrelevant for the description of the type of a posteriori error estimator considered here; thus we postpone the detailed presentation of the numerical method to Sect. 5.

The outline of the approach to a posteriori error estimation adopted here is as follows. Let us assume that a piecewise polynomial approximation u^h has been

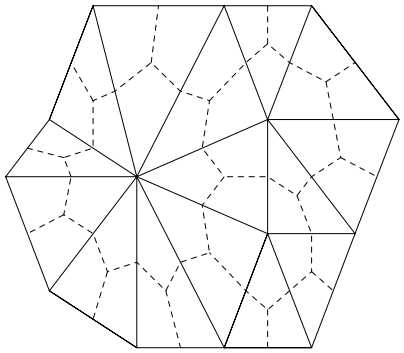

Fig. 1. Primary and secondary grid

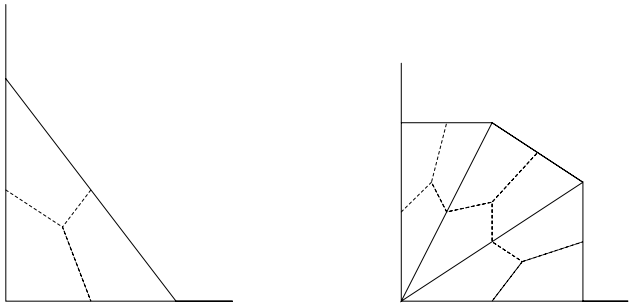

Fig. 2. Primary and secondary grid at boundaries

calculated on a space-time prism $P_{in} = (t_n, t_{n+1}) \times T_i$, where T_i is a a triangle in the primary grid. On each P_{in} we calculate, changing to entropy variables, the corresponding $U^h = U^h(u^h)$; substituting this into the linearised symmetrised Euler equations on P_{in} we calculate a local residual. In the next section we show that a suitable norm of the residual provides a two-sided bound on the error in the L^2-norm.

4 Residual-based a posteriori error estimation

In order to be able to derive a local a posteriori error bound, we first perform a localisation procedure based on decomposing the global error into a locally created part (called the cell error) whose size is controlled by the computable local residual, and a non-local propagating component (called the transported error) upon which the residual has no direct control.

4.1 Cell error and transported error

We consider, for a triangle $T_i \in \mathscr{T}$ and the associated space-time prism $P_{in} = (t_n, t_{n+1}) \times T_i$, the matrix

$$B(P_{in}) := \sum_{j=0}^{2} \hat{\nu}_j M_j = \sum_{j=0}^{2} \hat{\nu}_j A_j(u_{ci}) A^0(U_{ci})$$

where $\hat{\nu} = (\hat{\nu}_0, \hat{\nu}_1, \hat{\nu}_2)$ denotes the outer unit normal vector to ∂P_{in}. We shall suppose that $B(P_{in})$ is non-singular on ∂P_{in}; in other words, that ∂P_{in} is a non-characteristic hypersurface for the operator $\mathscr{L}$. We split B into a negative semi-definite part B^- and a positive semi-definite part $B^+ = B - B^-$. We call $B^- v$ the *inflow part* of a vector field v and $B^+ v$ its outflow part. Given a sufficiently smooth function g on ∂P_{in},

$$B^- V = B^- g \quad \text{on } \partial P_{in}$$

defines an admissible boundary condition for the symmetric hyperbolic problem (2.9), in the sense that, subject to this boundary condition, (2.9) has a unique strong solution (see [5] and [11]).

In order to proceed, we shall assume that we are given the numerical solution u^h on the space-time prism $P_{in} = (t_n, t_{n+1}) \times T_i$, where T_i is a triangle in the primary grid, and that we have calculated, converting to entropy variables, $U^h = U^h(u^h)$. Following [15], we consider the following boundary value problem on P_{in}:

$$\begin{aligned} \mathscr{L}\tilde{U}^h &= 0 \quad \text{on} \quad P_{in} \\ B^- \tilde{U}^h\big|_{\partial P_{in}} &= B^- U^h\big|_{\partial P_{in}}. \end{aligned}$$

We interpret the function $\tilde{U}^h$ as follows. Suppose that we have constructed an approximation U^h to the analytical solution U of (2.9). Then the boundary data $B^- U^h|_{\partial P_{in}}$ is distorted by numerical errors upwind of cell P_{in}. Thus, $\tilde{U}^h$ is the exact solution of (2.9) under these distorted boundary values. Consequently,

$$e^{\text{cell}}_{P_{in}} := U^h - \tilde{U}^h$$

is the error in the numerical solution which is produced on P_{in}, while

$$e^{\text{trans}}_{P_{in}} := \tilde{U}^h - U$$

is the error which is created upwind of the cell P_{in} and is advected into the cell by the numerical method. We call $e^{\text{cell}}_{P_{in}}$ the *cell error* and $e^{\text{trans}}_{P_{in}}$ the *transported error*. Clearly,

$$e_{P_{in}} = e^{\text{cell}}_{P_{in}} + e^{\text{trans}}_{P_{in}}.$$

It is important to note that the residual has no direct control over the transported error. Indeed, a simple calculation shows that

$$\mathscr{L} e^{\text{trans}}_{P_{in}} = \mathscr{L}\tilde{U}^h - \mathscr{L}U = 0,$$

subject to the boundary condition

$$B^- e^{\text{trans}}_{P_{in}} = B^-(U^h - U)\big|_{\partial P_{in}} = B^- e\big|_{\partial P_{in}},$$

while the cell error is governed directly by the residual via

$$r^h = \mathscr{L} e_{P_{in}} = \mathscr{L} e^{\text{cell}}_{P_{in}} \qquad \text{on } P_{in},$$

subject to the boundary condition

$$B^- e^{\text{cell}}_{P_{in}} = 0 \qquad \text{on } \partial P_{in}.$$

Now we are ready to proceed with the derivation of our local a posteriori error bound on $e^{\text{cell}}_{P_{in}}$ in terms of the computable local residual.

Note that the remarks of this section apply equally well to the non-symmetric system (2.8), where the corresponding boundary matrix is given by

$$\tilde{B}(P_{in}) = \sum_{j=0}^{2} \hat{\nu}_j \tilde{M}_j. \tag{4.1}$$

4.2 A weak a posteriori error estimate

We have shown above that, upon local linearisation about a constant state in a cell P_{in}, the symmetrised form of the Euler equations is a Friedrichs system. Let us therefore consider the following linear partial differential operator (slightly more general than required in order to deal with the constant-coefficient problem (2.9)) on a space-time prism $P_{in} = (t_n, t_{n+1}) \times T_i$ in the independent variables $x_0 = t$, x_1 and x_2:

$$\mathscr{L} v := \sum_{j=0}^{2} M_j(x) \partial_{x_j} v + C(x) v, \qquad x \in P_{in},$$

where the M_j and C are 4×4 matrices, the entries of each of the M_j being Lipschitz continuous on $\overline{P}_{in}$, and the entries of C being continuous functions on $\overline{P}_{in}$. We make the following additional assumptions:

i) for each P_{in} there exists a weight function $w_{in} \in C^1(\overline{P}_{in})$, positive on $\overline{P}_{in}$, and a positive constant c_{in} such that, for all $x \in \overline{P}_{in}$, in a pointwise sense,

$$\frac{1}{2}(K(x) + K^*(x)) \geq c_{in} I,$$

where

$$K := C + \sum_{j=0}^{2} \left(\partial_{x_j} \ln w_{in}\right) M_j - \frac{1}{2} \sum_{j=0}^{2} \partial_{x_j} M_j;$$

ii) $M_j(x) = M_j^*(x)$ for all $x \in \overline{P}_{in}$, $j = 0, 1, 2$.

Note that the condition on the symmetric part of K in i) is equivalent to the symmetric part of K being positive definite.

For the particular case of the symmetrised Euler equations, linearised about a constant state on P_{in}, the M_j are symmetric constant matrices and C is identically zero. We note that for symmetric *hyperbolic* systems, the case that we have been led to consider for the unsteady compressible Euler equations, the weight function can be taken to be

$$w_{in}(x) = \mathrm{e}^{\xi_{in}\cdot(x-x_{in}^{\mathrm{c}})},$$

where ξ_{in} is a local time-like direction on P_{in} (suitably scaled so as to satisfy hypothesis i) above), and x_{in}^{c} is the centroid of the space-time prism P_{in}.

Let

$$B(x) = \sum_{j=0}^{2} \hat{\nu}_j M_j(x),$$

and suppose that the matrix $B(x)$ is non-singular, almost everywhere on ∂P_{in}. Decomposing $B(x)$ as $B(x) = B^+(x) + B^-(x)$, where $B^+(x)$ is positive semi-definite on ∂P_{in}, $B^-(x)$ is negative semi-definite on ∂P_{in}, we consider the weighted graph-norm $\|\cdot\|_{D(\mathscr{L},P_{in})}$ on

$$D_-(\mathscr{L},P_{in}) := \{\phi \in L^2(P_{in}) \,|\, \mathscr{L}\phi \in L^2(P_{in}), \quad B^-\phi = 0 \text{ on } \partial P_{in}\},$$

defined by

$$\|\phi\|_{D(\mathscr{L},P_{in})} = (\|w_{in}\phi\|^2_{L^2(P_{in})} + \|w_{in}\mathscr{L}\phi\|^2_{L^2(P_{in})})^{1/2},$$

and the associated dual graph-norm

$$\|v\|_{D'(\mathscr{L},P_{in})} := \sup_{\phi\in D_-(\mathscr{L},P_{in})} \frac{|(v,\phi)_{P_{in}}|}{\|\phi\|_{D(\mathscr{L},P_{in})}},$$

where $(\cdot,\cdot)_{P_{in}}$ denotes the usual L^2 inner product on P_{in}. Similarly, by introducing the formal adjoint

$$\mathscr{L}^*\phi := -\sum_{j=0}^{2} \partial_{x_j}(M_j\phi) + C^*\phi,$$

with

$$\phi \in D_+(\mathscr{L}^*,P_{in}) := \{\phi \in L^2(P_{in}) \,|\, \mathscr{L}^*\phi \in L^2(P_{in}), \quad B^+\phi = 0 \text{ on } \partial P_{in}\},$$

we may equip $D_+(\mathscr{L}^*,P_{in})$ with the graph-norm

$$\|\phi\|_{D(\mathscr{L}^*,P_{in})} = (\|w_{in}\phi\|^2_{L^2(P_{in})} + \|w_{in}\mathscr{L}^*\phi\|^2_{L^2(P_{in})})^{1/2}.$$

The associated dual graph-norm is defined by

$$\|v\|_{D'(\mathscr{L}^*,P_{in})} := \sup_{\phi\in D_+(\mathscr{L}^*,P_{in})} \frac{|(v,\phi)_{P_{in}}|}{\|\phi\|_{D(\mathscr{L}^*,P_{in})}}.$$

The existence of the traces is not obvious and has to be proven. This was done in [15].

We have the following local a posteriori error bound for the L^2-norm of the cell error $e^{\text{cell}}_{P_{in}}$ on a space-time prism P_{in} in terms of the dual graph-norm of the local residual r^h.

Theorem 4.1. *Under hypotheses* i) *and* ii) *stated above,*

$$(\min_{P_{in}} w_{in})\,\|r^h\|_{D'(\mathscr{L}^*,P_{in})} \le \|e_{\mathrm{c}}\|_{L^2(P_{in})} \le \left(1+\frac{1}{c_{in}^2}\right)^{1/2} (\max_{P_{in}} w_{in})\,\|r^h\|_{D'(\mathscr{L}^*,P_{in})}.$$

Proof. In order to simplify the notation, we shall write e_{c} instead of $e^{\text{cell}}_{P_{in}}$ throughout this proof. To begin, we show that the graph norm $\|\cdot\|_{D(\mathscr{L}^*,P_{in})}$ is equivalent to the norm $\|w_{in}\mathscr{L}^*\cdot\|_{L^2(P_{in})}$ on $D_+(\mathscr{L}^*,P_{in})$. Then, in the second part of the proof, we shall use this result to deduce the stated two-sided bound on the cell error in terms of the dual graph-norm of the local residual.

A straightforward calculation based on integration by parts shows that, for any $\phi \in D_+(\mathscr{L}^*,P_{in})$,

$$\begin{aligned}(4.2)\quad \left(\partial_{x_j}(M_j\phi), w_{in}^2\phi\right)_{P_{in}} &= \frac{1}{2}\left(\hat{\nu}_j M_j\phi, w_{in}^2\phi\right)_{\partial P_{in}} \\ &\quad +\frac{1}{2}\left(\left(\partial_{x_j}M_j - M_j\partial_{x_j}(\ln w_{in}^2)\right)\phi, w_{in}^2\phi\right)_{P_{in}},\end{aligned}$$

for $j=0,1,2$, where $\hat{\nu}=(\hat{\nu}_0,\hat{\nu}_1,\hat{\nu}_2)$ denotes the unit outward normal to ∂P_{in}. To prove this equality we start from its right-hand side. It follows from integration by parts that

$$\begin{aligned}&\frac{1}{2}\left((\partial_{x_j}M_j)\phi, w_{in}^2\phi\right)_{P_{in}} - \frac{1}{2}\left((\partial_{x_j}w_{in}^2)M_j\phi,\phi\right)_{P_{in}} \\ &\quad = \frac{1}{2}\left(\hat{\nu}_j M_j\phi, w_{in}^2\phi\right)_{\partial P_{in}} - \left(M_j\phi, (\partial_{x_j}w_{in}^2)\phi + w_{in}^2(\partial_{x_j}\phi)\right)_{P_{in}}.\end{aligned}$$

Thus, the right-hand side of (4.2) becomes

$$\left(\hat{\nu}_j M_j\phi, w_{in}^2\phi\right)_{\partial P_{in}} - \left(M_j\phi, (\partial_{x_j}w_{in}^2)\phi + w_{in}^2(\partial_{x_j}\phi)\right)_{P_{in}}.$$

On the other hand, integration by parts on the left-hand side of (4.2) yields

$$\begin{aligned}\left(\partial_{x_j}(M_j\phi), w_{in}^2\phi\right)_{P_{in}} &= \left(\hat{\nu}_j M_j\phi, w_{in}^2\phi\right)_{\partial P_{in}} - \left(M_j\phi, \partial_{x_j}(w_{in}^2\phi)\right)_{P_{in}} \\ &= \left(\hat{\nu}_j M_j\phi, w_{in}^2\phi\right)_{\partial P_{in}} \\ &\quad - \left(M_j\phi, (\partial_{x_j}w_{in}^2)\phi + w_{in}^2(\partial_{x_j}\phi)\right)_{P_{in}}\end{aligned}$$

which proves (4.2). Thence, with

$$B = \sum_{j=0}^{2}\hat{\nu}_j M_j,$$

and $B^+ + B^- = B$, we have that

$$\left(\mathscr{L}^*\phi, w_{in}^2\phi\right)_{P_{in}} = \left(K^*\phi, w_{in}^2\phi\right)_{P_{in}} - \frac{1}{2}\sum_{j=0}^{2}\left(\hat{\nu}_j M_j\phi, w_{in}^2\phi\right)_{\partial P_{in}},$$

yielding

$$(\mathscr{L}^*\phi, w_{in}^2\phi)_{P_{in}} = (K^*\phi, w_{in}^2\phi)_{P_{in}} + \frac{1}{2}(-B^-\phi, w_{in}^2\phi)_{\partial P_{in}},$$

where we have made use of the fact that $B^+\phi = 0$ on ∂P_{in}. Now

$$\begin{aligned}(\mathscr{L}^*\phi, w_{in}^2\phi)_{P_{in}} &= \frac{1}{2}\left[(\mathscr{L}^*\phi, w_{in}^2\phi)_{P_{in}} + (w_{in}^2\phi, \mathscr{L}^*\phi)_{P_{in}}\right] \\ &= \frac{1}{2}\left((K + K^*)\phi, w_{in}^2\phi\right)_{P_{in}} + \frac{1}{2}(-B^-\phi, w_{in}^2\phi)_{\partial P_{in}}.\end{aligned}$$

Recalling that the matrix $-B^-$ is positive semi-definite and exploiting hypothesis i), we deduce that

$$(\mathscr{L}^*\phi, w_{in}^2\phi)_{P_{in}} \geq c_{in}\|w_{in}\phi\|^2_{L^2(P_{in})}.$$

Applying the Cauchy-Schwarz inequality on the left-hand side yields

$$\|w_{in}\mathscr{L}^*\phi\|_{L^2(P_{in})} \geq c_{in}\|w_{in}\phi\|_{L^2(P_{in})}.$$

Consequently,

$$\|\phi\|_{D(\mathscr{L}^*,P_{in})} \leq \left(1 + \frac{1}{c_{in}^2}\right)^{1/2}\|w_{in}\mathscr{L}^*\phi\|_{L^2(P_{in})}. \tag{4.3}$$

Since, by the definition of the graph norm,

$$\|w_{in}\mathscr{L}^*\phi\|_{L^2(P_{in})} \leq \|\phi\|_{D(\mathscr{L}^*,P_{in})}, \tag{4.4}$$

recalling (4.3) we obtain the two-sided bound

$$\|w_{in}\mathscr{L}^*\phi\|_{L^2(P_{in})} \leq \|\phi\|_{D(\mathscr{L}^*,P_{in})} \leq \left(1 + \frac{1}{c_{in}^2}\right)^{1/2}\|w_{in}\mathscr{L}^*\phi\|_{L^2(P_{in})}, \tag{4.5}$$

for any $\phi \in D_+(\mathscr{L}^*, P_{in})$. We shall exploit this pair of inequalities to derive a bound on the dual graph-norm of the residual r^h. Since

$$\begin{aligned}\mathscr{L}e_c &= r^h \quad \text{on } P_{in} \\ B^-e_c &= 0 \quad \text{on } \partial P_{in},\end{aligned}$$

it follows that

$$\begin{aligned}
\|r^h\|_{D'(\mathscr{L}^*,P_{in})} &= \sup_{\phi\in D_+(\mathscr{L}^*,P_{in})} \frac{|(\mathscr{L}e_c,\phi)_{P_{in}}|}{\|\phi\|_{D(\mathscr{L}^*,P_{in})}} \\
&= \sup_{\phi\in D_+(\mathscr{L}^*,P_{in})} \frac{|(e_c,\mathscr{L}^*\phi)_{P_{in}}|}{\|\phi\|_{D(\mathscr{L}^*,P_{in})}} \\
&= \sup_{\phi\in D_+(\mathscr{L}^*,P_{in})} \frac{|(w_{in}^{-1}e_c,w_{in}\mathscr{L}^*\phi)_{P_{in}}|}{\|\phi\|_{D(\mathscr{L}^*,P_{in})}} \\
&\le \sup_{\phi\in D_+(\mathscr{L}^*,P_{in})} \frac{\|w_{in}^{-1}e_c\|_{L^2(P_{in})}\|w_{in}\mathscr{L}^*\phi\|_{L^2(P_{in})}}{\|\phi\|_{D(\mathscr{L}^*,P_{in})}}.
\end{aligned}$$

Thus, by virtue of (4.4), we obtain

$$\|r^h\|_{D'(\mathscr{L}^*,P_{in})} \le \|w_{in}^{-1}e_c\|_{L^2(P_{in})} \le (\min_{P_{in}} w_{in})^{-1}\ \|e_c\|_{L^2(P_{in})},$$

and hence

$$(\min_{P_{in}} w_{in})\ \|r^h\|_{D'(\mathscr{L}^*,P_{in})} \le \|e_c\|_{L^2(P_{in})}, \tag{4.6}$$

which is the desired lower bound on the cell error. In order to prove the upper bound on the L^2-norm of the cell error, we consider the auxiliary problem

$$\begin{aligned}
\mathscr{L}^*\psi &= e_c \qquad \text{on } P_{in} \\
B^+\psi &= 0 \qquad \text{on } \partial P_{in};
\end{aligned}$$

this has a unique solution $\psi \in D_+(\mathscr{L}^*, P_{in})$ satisfying (4.5) (see [11]). Thus,

$$\begin{aligned}
\|r^h\|_{D'(\mathscr{L}^*,P_{in})} &= \sup_{\phi\in D_+(\mathscr{L}^*,P_{in})} \frac{|(\mathscr{L}e_c,\phi)_{P_{in}}|}{\|\phi\|_{D(\mathscr{L}^*,P_{in})}} \\
&= \sup_{\phi\in D_+(\mathscr{L}^*,P_{in})} \frac{|(e_c,\mathscr{L}^*\phi)_{P_{in}}|}{\|\phi\|_{D(\mathscr{L}^*,P_{in})}} \\
&\ge \frac{|(e_c,\mathscr{L}^*\psi)_{P_{in}}|}{\|\psi\|_{D(\mathscr{L}^*,P_{in})}} \\
&= \frac{\|e_c\|_{L^2(P_{in})}\|\mathscr{L}^*\psi\|_{L^2(P_{in})}}{\|\psi\|_{D(\mathscr{L}^*,P_{in})}} \\
&= \frac{\|e_c\|_{L^2(P_{in})}\|w_{in}^{-1}w_{in}\mathscr{L}^*\psi\|_{L^2(P_{in})}}{\|\psi\|_{D(\mathscr{L}^*,P_{in})}} \\
&\ge (\max_{P_{in}} w_{in})^{-1}\frac{\|e_c\|_{L^2(P_{in})}\|w_{in}\mathscr{L}^*\psi\|_{L^2(P_{in})}}{\|\psi\|_{D(\mathscr{L}^*,P_{in})}}.
\end{aligned}$$

Recalling (4.3), it follows that

$$\|r^h\|_{D'(\mathscr{L}^*,P_{in})} \ge \left(1+\frac{1}{c_{in}^2}\right)^{-1/2} (\max_{P_{in}} w_{in})^{-1}\|e_c\|_{L^2(P_{in})},$$

which yields the required upper bound on the L_2-norm of the cell error in terms of the dual graph norm of the local residual r^h. □

The sharpness of the cell error estimate stated in Theorem 4.1 depends on the size of c_{in}, as well on $\min_{P_{in}} w_{in}$ and $\max_{P_{in}} w_{in}$. Choosing $w_{in}(x) = \mathrm{e}^{\xi_{in}\cdot(x-x_{in}^{\mathrm{c}})}$, with ξ_{in} a local time-like direction on P_{in} and x_{in}^{c} the centroid of P_{in}, it follows that $w_{in}(x) = 1 + \mathscr{O}(\mathrm{diam}(P_{in}))$, which implies that w_{in} is close to unity on each P_{in}. For unsteady problems ξ is chosen as the time-direction, while for steady problems it is taken to be a local time-like direction.

The next section is devoted to the practical implementation of the two-sided error bound stated in Theorem 4.1 into the DLR-τ-Code for the numerical solution of the compressible Euler equations.

5 The DLR-τ-code

We aim at describing the implementation of the dual graph norm error indicator in the framework of the DLR-τ-Code. We report briefly on the design and the features of the code and describe the adaptive techniques used.

5.1 Cell averages, finite volume approximations and recovery functions

We consider weak solutions of the Euler equations on the boxes B_i of a given triangulation, i.e. we identify the boxes B_i of the secondary grid with control volumes. The cell average operator on box B_i is defined as

$$\mathfrak{A}(B_i)u(t) := \frac{1}{|B_i|}\int_{B_i} u(x,t)\,dx.$$

Thus, on each box B_i the cell average of a weak solution u satisfies the evolution equation

$$\frac{d}{dt}\mathfrak{A}(B_i)u(t) = -\frac{1}{|B_i|}\oint_{\partial B_i}\sum_{i=1}^{2} f_i(u)\hat{\nu}_i\,ds.$$

Introducing a numerical flux function

$$S\times S\times\mathbb{R}^2 \ni u, v, \hat{\nu} \overset{H}{\longmapsto} H(u,v;\hat{\nu}) \in \mathbb{R}^4$$

satisfying the fundamental consistency condition

$$\forall v\in S: \quad H(v,v;\hat{\nu}) = \sum_{i=1}^{2} f_i(v)\hat{\nu}_i$$

leads, for smooth solutions, to

$$\frac{d}{dt}\mathfrak{A}(B_i)u(t) = -\frac{1}{|B_i|}\oint_{\partial B_i} H(u,u;\hat{\nu})\,ds.$$

If we denote the set of indices of neighbouring boxes to box B_i by $N(i)$, and the two segments of $B_i\cap B_j, j\in N(i)$, by $l_{ij}^k, k=1,2$, see Fig. 3, we arrive at

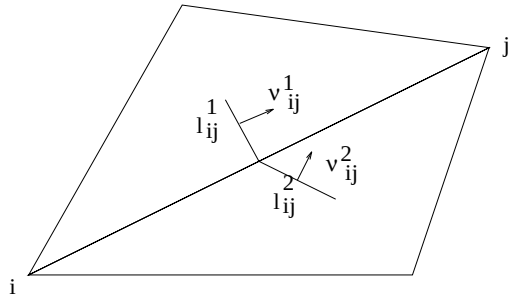

Fig. 3. Box boundary

$$\frac{d}{dt}\mathfrak{A}(B_i)u(t) = -\frac{1}{|B_i|}\sum_{j\in N(i)}\sum_{k=1}^{2}\int_{l_{ij}^k} H(u,u;\hat{\nu}_{ij}^k)\,ds,$$

$\hat{\nu}_{ij}^k$ denoting the outer unit normal vector at l_{ij}^k with respect to B_i. Applying one-point Gaussian quadrature to the integral yields

$$\frac{d}{dt}\mathfrak{A}(B_i)u(t) = -\frac{1}{|B_i|}\sum_{j\in N(i)}\sum_{k=1}^{2} H\left(u(x_{ij}^k,t),u(x_{ij}^k,t);\hat{\nu}_{ij}^k\right)\left|l_{ij}^k\right| + \mathcal{O}(h^2)$$

where x_{ij}^k denotes the centre of l_{ij}^k. Note that the error due to the Gaussian quadrature is proportional to h^2.

A basic approximation which is at the heart of finite volume methods consists of replacing the point values $u(x_{ij}^k,t)$ by the cell averages on B_i and B_j, respectively.

Definition 5.1. The system of ordinary differential equations

$$\begin{aligned}\frac{d}{dt}\overline{u}_i(t) &= -\frac{1}{|B_i|}\sum_{j\in N(i)}\sum_{k=1}^{2} H\left(\overline{u}_i(t),\overline{u}_j(t);\hat{\nu}_{ij}^k\right)\left|l_{ij}^k\right| \\ \overline{u}_i(t) &:= \mathfrak{A}(B_i)u(0)\end{aligned}$$

is called the basic finite volume approximation to (2.1).

To prove a formal order of accuracy of the basic finite volume approximation we need a result concerning the approximation properties of the cell average operator.

Lemma 5.1. *Let c_i denote the barycenter of box B_i. Then the approximation properties*

1. $\mathfrak{A}(B_i)u(t) = u(c_i,t) + \mathcal{O}(h^2)$,
2. $\mathfrak{A}(B_i)u(t) = u(x,t) + \mathcal{O}(h), \quad x \neq c_i$

are valid.

Proof. Let u^j denote a generic component of u. Taylor expansion about c_i yields

$$u^j(x,t) = \sum_{\mu=0}^{r-1} \frac{1}{\mu!} \sum_{|\alpha|=\mu} (x-c_i)^\alpha \partial^\alpha u^j \big|_{x=c_i} + \mathscr{O}(h^r)$$

for any $r \in \mathbb{N}$. If the cell average operator is applied and $r = 2$ is chosen then

$$\mathfrak{A}(B_i)u^j(t) = u^j(c_i,t) + \frac{1}{|B_i|} \int_{B_i} (x-c_i)\,dx \cdot \nabla_x u^j(x,t)|_{x=c_i} + \mathscr{O}(h^2)$$

holds. Now

$$c_i = \frac{1}{|B_i|} \int_{B_i} x\,dx$$

by the definition of the barycenter, which proves (1). Statement (2) follows along the same lines by expanding about $x \neq c_i$. □

Using Taylor expansion again and noting that the use of the one-point Gaussian quadrature rule has an error of order $\mathscr{O}(h^2)$ it is easily seen that the following result holds.

Theorem 5.1. *Assuming u and H to be smooth, the basic finite volume approximation is of spatial order $\mathscr{O}(h)$ in the sense that*

$$H(\overline{u}_i(t), \overline{u}_j(t); \hat{\nu}_{ij}^k) = \sum_{l=1}^{2} f_l\left(u(x_{ij}^k, t)\right) \hat{\nu}_{ij,l}^k + \mathscr{O}(h).$$

Note that one cannot establish an order of accuracy $\mathscr{O}(h)$ in the sense of $\sum_{\ell=1}^{2} \partial_{x_\ell} f_\ell(u) = \frac{1}{|B_i|} \sum_{j \in N(i)} \sum_{k=1}^{2} H(\overline{u}_i(t), \overline{u}_j(t); \hat{\nu}_{ij}^k)|l_{ij}^k| + \mathscr{O}(h)$, since supraconvergence phenomena occur on unstructured grids, see [6].

To increase the spatial order of accuracy we use the theory of recovery as developed and described in [19]. Suppose on box B_i a linear polynomial

$$p_i^u(x) := a_{00}^i + a_{10}^i(x_1 - c_{i,1}) + a_{01}^i(x_2 - c_{i,2})$$

has to be recovered from cell average data (at each time level t, which we drop for simplicity). In order to preserve cell averages we insist on

$$\mathfrak{A}(B_i)p_i^u = \mathfrak{A}(B_i)u,$$

which, since $\mathfrak{A}(B_i)x = c_i$, yields

$$a_{00}^i \equiv \overline{u}_i.$$

Thus, the recovery of a linear polynomial reduces to the recovery of a gradient

$$\nabla_x p_i^u = (a_{10}^i, a_{01}^i).$$

Consider the recovery problem on box B_i and let T be a triangle with node x_i according to Fig. 4, i.e. $T \in K_{h,i}$. On T we consider the space $\Pi_1(T)$ of linear polynomials with basis $\{\varphi_i, \varphi_j, \varphi_k\}$ characterised by the conditions

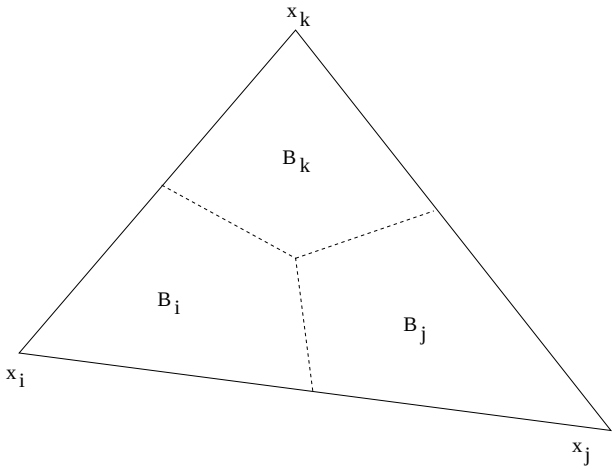

Fig. 4. Generic triangle $T \in K_{h,i}$

$$\varphi_l(x_m) = \delta_l^m, \quad l, m \in \{i, j, k\},$$

and we define the Lagrange interpolant of the cell averages as

$$u_T^h(x) := \overline{u}_i \varphi_i(x) + \overline{u}_j \varphi_j(x) + \overline{u}_k \varphi_k(x).$$

For each triangle $T \in K_{h,i}$ we compute $\nabla_x u_T^h$ which is a constant vector on T. We then define

$$\nabla_x p_i^u := \nabla_x u_{\tilde{T}}^h, \quad \left|\nabla_x u_{\tilde{T}}^h\right| = \min_{T \in K_{h,i}} \left|\nabla_x u_T^h\right|,$$

i.e. the smallest gradient of the Lagrangien interpolants on the triangles around node i is assigned to be the gradient on box B_i.

Instead of using the piecewise constant cell averages, which have poor approximation properties, as arguments in the numerical flux function we now use the value of the p_l^u at the midpoint x_{ij}^k of the edges of neighbouring boxes. The final finite volume approximation is then described by the system of ordinary differential equations

$$\frac{d}{dt}\overline{u}_i(t) = -\frac{1}{|B_i|} \sum_{j \in N(i)} \sum_{k=1}^{2} H\left(p_i^u(x_{ij}^k, t), p_j^u(x_{ij}^k, t); \hat{\nu}_{ij}^k\right) \left|l_{ij}^k\right| \tag{5.1}$$

$$\overline{u}_i(0) = \mathfrak{A}(B_i) u(0). \tag{5.2}$$

We remark that within the DLR-τ-code the primitive variables ρ, v_1, v_2, p are recovered instead of the conservative variables u. From recovered primitive data, the values of conservative data are easily computed at the point x_{ij}^k.

We can show by a simple Taylor expansion in the variables of the numerical flux function that the finite volume approximation (5.1) is spatially consistent of the order $\mathcal{O}(h^2)$ in the sense of Theorem 5.1. This is by no means equivalent to

second order convergence of the scheme which we indeed can not prove due to the inherent nonlinearity of the problem and the discretisation.

We want to concentrate on explicit time stepping schemes, for simplicity, i.e. the right-hand side of (5.1) is evaluated at time level $t = n + \Delta t$, $n \in \mathbb{N}$, while the left-hand side is discretised so that an explicit formula for $\overline{u}_i((n+1)\Delta t)$ can be derived. The simplest scheme of this kind is given by

$$\frac{\overline{u}_i((n+1)\Delta t) - \overline{u}_i(n\Delta t)}{\Delta t} = \frac{d}{dt}\overline{u}_i(t) + \mathcal{O}(\Delta t)$$

which is what we shall exploit in the experiments. Note that a severe Courant-Friedrichs-Lewy (CFL) stability condition has to be satisfied with this simple discretisation. We used, on each box B_i,

$$\frac{\Delta t_i}{S_i} \leq \max_{l_{ij}^k}\{|ev(A(\overline{u}_i, \hat{\nu}_{ij}^k))|\}$$

where S_i denotes the shortest distance from the barycentre of B_i to its boundary and $ev(A)$ the set of eigenvalues of A. For time accurate computations the minimum

$$\Delta t := \min_i \Delta t_i$$

is chosen as global time step. For more sophisticated explicit time stepping schemes used in the DLR-τ-code see [20]. Implicit schemes are considered in depth in [17], see also [4].

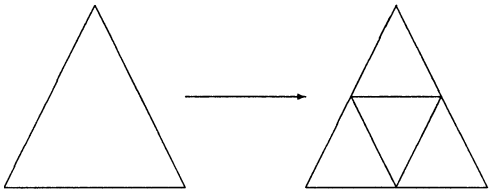

Fig. 5. Red refinement

5.2 Adaptive techniques

Of the several different strategies that were tested in the past and documented in [21], [22], [9], an isotropic red-green refinement, following ideas of Bank et al. [1] and Kornhuber and Roitzsch [14], seems to be most appropriate.

The red refinement of a triangle is shown in Fig. 5. If a set of triangles is red-refined the resulting hanging nodes can be removed through the green refinement shown in Fig. 6. Obviously the red refinement is harmless because it splits a triangle into four geometrically similar subtriangles. In contrast, the green refinement may lead to triangles with very small angles. To ensure stability of the algorithm we use a procedure described by Kornhuber and Roitzsch [14]. At the beginning of each refinement step all green refinements are removed from

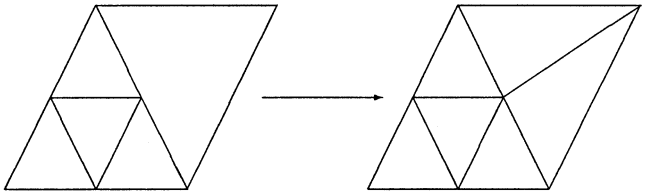

Fig. 6. Green refinement

the grid. After red-refining all triangles that have to be refined due to information of the refinement indicator, all triangles with more than one hanging node are also red-refined. In a final phase the remaining hanging nodes are removed by means of the green refinement.

If the refinement indicator signals that a triangle has to be removed from the triangulation a coarsening procedure developed by Hempel [10] is used. This procedure is able to remove successively all levels of refinement down to the initial grid and is based on local considerations concerning the triangles which share a common point.

5.3 Remarks concerning the finite volume approximation

It should be noted that the finite volume code described previously numerically solves the Euler equations in *conserved* variables and not in *entropy* variables. Since our considerations concerning the error indicator are based on entropy variables we have two distinct ways of implementing the dual graph-norm indicator. We could have re-written the code in terms of entropy variables and then consistently work only in this set of variables. This approach would have been far from practical since virtually all numerical methods for the Euler equations rely on conserved variables due to their physical significance. Our approach stays with the finite volume approximation of the Euler equations in conserved variables. In the initial step of the adaptive process our conservative data is transformed to entropy variables. It is in this sense that the hypotheses i) and ii) of Subsect. 4.2 are satisfied since the matrices occuring in the transformed system satisfy these conditions. The Euler equations in conserved variables do not satisfy the hypotheses. Since it is well known that the system in entropy variables have the same weak solutions as the systems in conserved variables a transformation between these sets of variables does not do harm to the numerical solution.

6 The implementation of the dual graph norm indicator

There are in principle two different strategies for the implementation of the dual graph norm indicator: both of them are based on approximating $\|r^h\|_{D'(\mathscr{S}^*,P_{in})}$ using a subdivision of P_{in}. On a particular subdivision we exploit a finite element basis $\{\Phi\}$ that satisfies the local boundary condition $B^+\Phi = 0$ on ∂P_{in}. We start by

describing the imposition of boundary conditions. In order to derive an applicable error indicator we start with the non-symmetric system (2.8) which is nothing but the symmetric system (2.7) in a form more convenient for computational purposes.

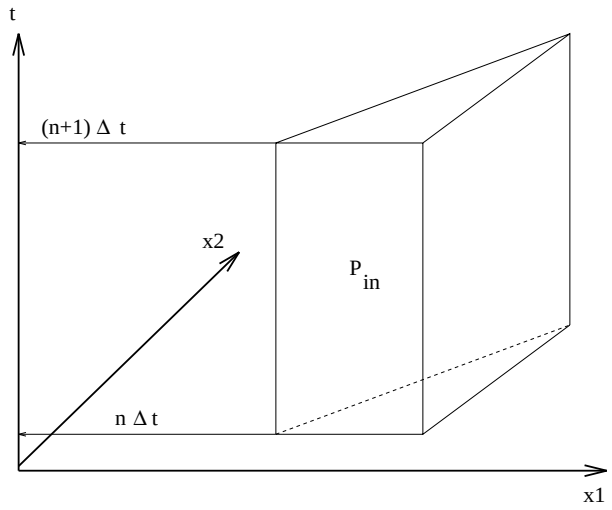

Fig. 7. Space-time prism P_{in}

6.1 Boundary conditions

Consider a space-time prism P_{in} as in Fig. 7. Recall that the boundary condition matrix (4.1) for system (2.8) is given by

$$\begin{aligned}\tilde{B}(P_{in}) = \sum_{j=0}^{2} \hat{\nu}_j \tilde{M}_j &= \sum_{j=0}^{2} \hat{\nu}_j A^{0^{-1}}(U_{ci}) A_j(u_{ci}) A^0(U_{ci}) \\ &= \hat{\nu}_0 I + \sum_{j=1}^{2} \hat{\nu}_j A^{0^{-1}}(U_{ci}) A_j(u_{ci}) A^0(U_{ci}),\end{aligned}$$

where U_{ci}, u_{ci} denote constant mean states of entropy and conservative variables, respectively, within the prism P_{in}.

In order to distinguish inflow from outflow boundaries the matrix $\tilde{B}(P_{in})$ is split into a positive semi-definite part $\tilde{B}^+(P_{in})$, the outflow part, and a negative semi-definite part $\tilde{B}^-(P_{in})$, the inflow part, so that

$$\tilde{B}(P_{in}) = \tilde{B}^+(P_{in}) + \tilde{B}^-(P_{in}).$$

Since the matrices $\tilde{M}_j$ are similar to A_j, for $j = 1, 2$, and $\tilde{M}_0$ is similar to I, the set of eigenvalues of $\tilde{B}(P_{in})$ is given by

$$ev(\tilde{B}(P_{in})) = \hat{\nu}_0 + ev\left(\sum_{j=1}^{2} \hat{\nu}_j A_j(u_{ci})\right).$$

Now it is well known (see [3]) that there exists an invertible matrix $P(u_{ci}, \hat{\nu}_1, \hat{\nu}_2) \in \mathbb{R}^{4\times 4}$ such that

$$P(u_{ci}, \hat{\nu}_1, \hat{\nu}_2)^{-1}\left(\sum_{j=1}^{2} \hat{\nu}_j A_j(u_{ci})\right) P(u_{ci}, \hat{\nu}_1, \hat{\nu}_2) = \Lambda(u_{ci}, \hat{\nu}_1, \hat{\nu}_2),$$

where Λ is the diagonal matrix

$$\begin{aligned}\Lambda(u_{ci}, \hat{\nu}_1, \hat{\nu}_2) \quad = \quad & \operatorname{diag}\left\{\sum_{j=1}^{2} \hat{\nu}_j v_{ci,j}, \sum_{j=1}^{2} \hat{\nu}_j v_{ci,j}, \sum_{j=1}^{2} \hat{\nu}_j v_{ci,j} + a_{ci}|(\hat{\nu}_1, \hat{\nu}_2)|,\right. \\ & \left.\sum_{j=1}^{2} \hat{\nu}_j v_{ci,j} - a_{ci}|(\hat{\nu}_1, \hat{\nu}_2)|\right\},\end{aligned}$$

$a_{ci} := \sqrt{\kappa \frac{p_{ci}}{\rho_{ci}}}$ denoting the mean constant speed of sound in P_{in}. We split Λ into a matrix Λ^+ containing the positive eigenvalues, and Λ^- containing the negative eigenvalues, i.e.

$$\Lambda(u_{ci}, \hat{\nu}_1, \hat{\nu}_2) = \Lambda^+(u_{ci}, \hat{\nu}_1, \hat{\nu}_2) + \Lambda^-(u_{ci}, \hat{\nu}_1, \hat{\nu}_2).$$

Thus, $\sum_{j=1}^{2} \hat{\nu}_j A_j(u_{ci})$ can be represented as a sum of a positive semi-definit and a negative semi-definite part, i.e.

$$\sum_{j=1}^{2} \hat{\nu}_j A_j(u_{ci}) = P\lambda^+ P^{-1}(u_{ci}, \hat{\nu}_1, \hat{\nu}_2) + P\lambda^- P^{-1}(u_{ci}, \hat{\nu}_1, \hat{\nu}_2)$$

and we end up with a representation for the boundary matrix $B(P_{in})$ of the form

$$\begin{aligned}\tilde{B}(P_{in}) = \hat{\nu}_0 I \quad & + \quad A^{0^{-1}}(U_{ci})\left(P\Lambda^+ P^{-1}(u_{ci}, \hat{\nu}_1, \hat{\nu}_2)\right) A^0(U_{ci}) \\ & + \quad A^{0^{-1}}(U_{ci})\left(P\Lambda^- P^{-1}(u_{ci}, \hat{\nu}_1, \hat{\nu}_2)\right) A^0(U_{ci}).\end{aligned}$$

Note that on the bottom face $T_i \cap \{n\Delta t\}$ of the space-time prism P_{in} there holds $\hat{\nu} = (-1, 0, 0)$ and thus

$$\tilde{B}(P_{in}) = -I = \tilde{B}^-(P_{in}).$$

Therefore, the bottom face is an inflow boundary of P_{in}. Analogously, on the top face $T_i \cap \{(n+1)\Delta t\}$ we have $\hat{\nu} = (1, 0, 0)$ and thus

$$\tilde{B}(P_{in}) = I = \tilde{B}^+(P_{in}),$$

i.e. this is an outflow face. On the three side faces of P_{in}, $\hat{\nu}_0 = 0$ is valid and thus $\tilde{B}(P_{in})$ is split according to the signs of eigenvalues in Λ. Note that this corresponds to the flux vector splitting of Steger and Warming, see [23]. Thus,

if $\phi \in D_+(\mathscr{S}^*, P_{in})$ is sought then the components of ϕ have to be chosen in order to cancel the expression

$$\tilde{B}^+(P_{in})\phi = 0$$

on the face under consideration. This is achieved by splitting Λ according to $\Lambda = \Lambda^+ + \Lambda^-$ and looking for ϕ which satisfy the condition

$$\Lambda^+\phi = 0.$$

6.2 The error indicator

As was already noted, two different strategies exist in principle for setting up the graph norm error indicator. In both approaches the space-time prisms P_{in} have to be subdivided and a finite set of test functions ϕ has to be defined on this subdivision. In the first approach one uses test functions $\phi \in D_+(\mathscr{S}^*, P_{in})$ in linear-linear tensor product form

$$\phi(x,t) = \alpha_{000} + \alpha_{100}t + \alpha_{010}x_1 + \alpha_{001}x_2 + \alpha_{110}x_1t + \alpha_{101}x_2t,$$

compare [2]. On T_i the Lagrange interpolants $u^h_{T_i}$ of the cell averages are computed at times $n\Delta t$ and $(n+1)\Delta t$ and u_{ci} is defined to be the average of the six values of $u^h_{T_i}$ at the nodes of T_i at the two time levels. Using quadrature rules the dual graph norm of the residual may be computed within P_{in} on the partition of the space-time prisms.

For the sake of simplicity and to save computing time we shall exploit an alternative to this approach which seems to be better suited to explicit time stepping schemes. We aim to compute the dual graph norm indicator from data which is available at time $n\Delta t$. Note that after one flux balance we know not only the values $\overline{u}_l(n\Delta t)$ but also the values of the temporal change

$$\frac{\overline{u}_l((n+1)\Delta t) - \overline{u}_l(n\Delta t)}{\Delta t} = Q_l,$$

where Q_l denotes the spatial finite volume discretisation. On triangle T_i a subdivision of the form shown in Fig. 8 is established and we assume our test functions to be constant in time, piecewise linear in space, i.e. of the form

$$\phi(x,t) = \phi(x) = \alpha_{00} + \alpha_{10}x_1 + \alpha_{01}x_2.$$

The subdivision of T_i gives rise to 15 different test functions $\phi_k, k = 1, \ldots, 15$, which we define to be the linear hat functions characterised by $\phi_k(x_j) = \delta^k_j$. To take into account the boundary conditions we proceed as follows. If element λ^+_{ll} of Λ^+ is non-zero at one of the boundary points on ∂T_i the corresponding component of ϕ_k, i.e. $\phi_{k,l}$, is set to zero so that $\Lambda^+\phi_k = 0$ holds for all ϕ_k. Obviously, $\phi_k \in D_+(\mathscr{S}^*, P_{in})$. Thus, the dual graph norm is approximated by

$$\|r^h\|_{D'(\mathscr{S}^*, P_{in})} \approx \max_{k=1,\ldots,15} \frac{|(r^h, \phi_k)_{P_{in}}|}{\|\phi_k\|_{D(\mathscr{S}^*, P_{in})}},$$

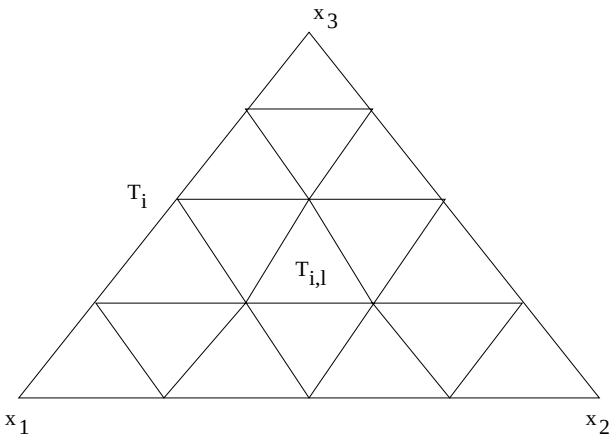

Fig. 8. Local subdivision of triangle T_i

with ϕ_k as previously defined. To compute the numerator and the denominator in the approximated dual graph norm we choose the mean constant state in P_{in} to be

$$u_{ci} := \frac{1}{3}(\overline{u}_1(n\Delta t) + \overline{u}_2(n\Delta t) + \overline{u}_3(n\Delta t)), \tag{6.1}$$

where the nodes of T_i are labelled 1,2,3 for simplicity. Note that this gives an $\mathcal{O}(\Delta t)$-approximation to a mean constant state which also includes the values at time level $(n+1)\Delta t$, provided we assume smoothness of the solution. Thus,

$$v(x,t) = u^h(x, n\Delta t)|_{T_i} - u_{ic} \tag{6.2}$$

is identified as linear perturbation of the mean constant state at time $[n\Delta t, (n+1)\Delta t]$. From (6.1) the mean constant state of entropy variabels U_{ci} is computed using (2.5) and from (6.2) the linear perturbation

$$V(x,t) = U(x,t)|_{T_i} - U_{ci}, \quad t \in [n\Delta t, (n+1)\Delta t],$$

follows. According to (2.9) the residual is now computed from

$$r^h = \mathcal{L}V = \partial_t V + \sum_{j=1}^{2} A^{0^{-1}}(U_{ci}) A_i(u_{ci}) A^0(U_{ci}) \partial_{x_i} V.$$

Taking the L^2-inner product with our test functions $\phi_k \in D_+(\mathcal{L}^*, P_{in})$ leads to

$$\begin{aligned}(r^h, \phi_k)_{P_{in}} \quad = \quad & \int_{T_i} \int_{n\Delta t}^{(n+1)\Delta t} \partial_t V \cdot \phi_k \, dt \, dx \\ & + \sum_{j=1}^{2} A^{0^{-1}}(U_{ci}) A_j(u_{ci}) A^0(U_{ci}) \int_{T_i} \int_{n\Delta t}^{(n+1)\Delta t} \partial_{x_j} V \cdot \phi_k \, dt \, dx.\end{aligned}$$

In order to stay at the n-th time level in the spatial part we use a simple one-point quadrature rule where the quadrature point is $n\Delta t$. This gives

$$\begin{aligned}(r^h,\phi_k)_{P_{in}} &= \int_{T_i}\phi_k(x)\cdot(V(x,(n+1)\Delta t)-V(x,n\Delta t))\,dx\\ &\quad+\sum_{j=1}^{2}A^{0^{-1}}(U_{ci})A_j(u_{ci})A^0(U_{ci})\Delta t\int_{T_i}\partial_{x_j}V(x,n\Delta t)\cdot\phi_k(x)\,dx\\ &\quad+\mathscr{O}(\Delta t^2).\end{aligned}$$

For each of the nodes $x_l, l=1,2,3$, of the triangle T_i we know the value Q_l of

$$\frac{\overline{u}_l((n+1)\Delta t)-\overline{u}_l(n\Delta t)}{\Delta t}=Q_l.$$

Since Q_l can be expressed as the difference of conservative variables we can switch to entropy data by means of transformation (2.5) yielding

$$\begin{aligned}\overline{U}_l &:= U(\overline{u}_l((n+1)\Delta t))-U(\overline{u}_l(n\Delta t))\\ &= U(\overline{u}_l(n\Delta t)+\Delta t Q_l)-U(\overline{u}_l(n\Delta t))\end{aligned}$$

The linear interpolant of $\overline{U}_l$ on T_i given by

$$U^h_{T_i}(x):=\sum_{l=1}^{3}\overline{U}_l\varphi_l(x),$$

$\varphi_l(x_m)=\delta^m_j$, can be calculated and this yields the linear perturbation

$$V^h_{T_i}(x):=U^h_{T_i}(x)-U_{ci}=\sum_{l=1}^{3}\overline{U}_l\varphi_l(x)-U_{ci}$$

in entropy variables. Thus, the time difference $V(x,(n+1)\Delta t)-V(x,n\Delta t)$ can be replaced by a transformed spatial flux balance resulting in

$$\begin{aligned}(r^h,\phi_k)_{P_{in}} &\doteq \int_{T_i}\phi_k(x)\cdot V^h_{T_i}(x)\,dx\\ &\quad+\sum_{j=1}^{2}A^{0^{-1}}(U_{ci})A_j(u_{ci})A^0(U_{ci})\Delta t\int_{T_i}\partial_{x_j}V(x,n\Delta t)\cdot\phi_k(x)\,dx\end{aligned}$$

where we introduce the symbol $\doteq$ meaning equality up to terms of order $\mathscr{O}(\Delta t^2, h|T_i|)$. Now $\partial_{x_j}V$ is a constant on T_i and can be removed from the integral. Since $T_i=\cup_{l=1}^{16}T_{i,l}$ and $|T_{i,l}|=|T_i|/16$ we arrive at

$$\begin{aligned}(r^h,\phi_k)_{P_{in}} &\doteq \sum_{l=1}^{16}\int_{T_{i,l}}\phi_k(x)\cdot V^h_{T_i}(x)\,dx\\ &\quad+\sum_{j=1}^{2}A^{0^{-1}}(U_{ci})A_j(u_{ci})A^0(U_{ci})\Delta t\;\partial_{x_j}V\big|_{T_i}\sum_{l=1}^{16}\int_{T_{i.l}}\phi_k(x)\,dx.\end{aligned}$$

If we apply the one-point quadrature rule in each subtriangle $T_{i,l}$ we finally end up with

$$\begin{aligned}(r^h, \phi_k)_{P_{in}} &\doteq \frac{|T_i|}{16}\sum_{l=1}^{16}\phi_k(c_{i,l})\cdot V_{T_i}^h(c_{i,l}) \\ &\quad + \sum_{j=1}^{2} A^{0^{-1}}(U_{ci})A_j(u_{ci})A^0(U_{ci})\Delta t\ \partial_{x_j}V\big|_{T_i}\frac{|T_i|}{16}\sum_{l=1}^{16}\phi_k(c_{i,l}).\end{aligned}$$

The denominator in the dual graph norm indicator is given by

$$\|\phi_k\|_{D(\mathscr{L}^*,P_{in})} = \sqrt{\|w_{in}\phi_k\|^2_{L^2(P_{in})} + \|w_{in}\mathscr{L}^*\phi_k\|^2_{L^2(P_{in})}}$$

where $w_{in}(x) = \mathrm{e}^{\xi_{in}\cdot(x-x_{in}^c)}$ is the local scaling (weight) function. Note that using this weight function with the time-like direction ξ_{in} ensures that hypotheses i) in Subsect. 4.2 holds. We have

$$\|w_{in}\phi_K\|^2_{L^2(P_{in})} = \int_{T_i}\int_{n\Delta t}^{(n+1)\Delta t}(w_{in}\phi_k)^2\,dt\,dx = \int_{T_i}\phi_k^2\int_{n\Delta t}^{(n+1)\Delta t} w_{in}^2\,dt\,dx$$

since our test functions were assumed to be constant in time. Using a one-point quadrature in the space-time barycenter x_{in}^c yields

$$\|w_{in}\phi_k\|^2_{L^2(P_{in})} \doteq \Delta t\int_{T_i}\phi_k^2\,dx \doteq \Delta t\sum_{l=1}^{16}\int_{T_{i,l}}\phi_k^2\,dx \doteq \frac{|T_i|}{16}\sum_{l=1}^{16}\big(\phi_k(c_{i,l})\big)^2.$$

The formal adjoint of the linearised operator

$$\mathscr{L} = \partial_t + \sum_{j=1}^{2} A^{0^{-1}}(U_{ci})A_j(u_{ci})A^0(U_{ci})\partial_{x_j}$$

is simply given by

$$\mathscr{L}^* = -\mathscr{L}.$$

Thus,

$$\|w_{in}\mathscr{L}^*\phi_k\|^2_{L^2(P_{in})} = \int_{T_i}\int_{n\Delta t}^{(n+1)\Delta t}\big(w_{in}\mathscr{L}\phi_k\big)^2\,dt\,dx.$$

Since ϕ_k are assumed not to change with time within P_{in} we arrive at

$$\begin{aligned}\|w_{in}\mathscr{L}^*\phi_k\|^2_{L^2(P_{in})} &= \int_{T_i}\left(\sum_{j=1}^{2}A^{0^{-1}}(U_{ci})A_j(u_{ci})A^0(U_{ci})\partial_{x_j}\phi_k\right)^2\times \\ &\quad \int_{n\Delta t}^{(n+1)\Delta t} w_{in}^2\,dt\,dx \\ &\doteq \Delta t\int_{T_i}\left(\sum_{j=1}^{2}A^{0^{-1}}(U_{ci})A_j(u_{ci})A^0(U_{ci})\partial_{x_j}\phi_k\right)^2 dx\end{aligned}$$

where the time integral was again approximated by a one-point rule with quadrature point x_{in}^c. Thus, we end up with

$$\|w_{in}\mathscr{L}^*\phi_k\|^2_{L^2(P_{in})} \doteq \Delta t\,\frac{|T_i|}{16}\sum_{l=1}^{16}\left(\sum_{j=1}^{2}A^{0^{-1}}(U_{ci})A_j(u_{ci})A^0(U_{ci})\partial_{x_j}\phi_k(c_{i,l})\right)^2.$$

Gathering our partial approximations gives
(6.2)

$$\|r^h\|_{D'(\mathscr{L}^*,P_{in})} \approx \|r^h\|_{\Delta'(\mathscr{L}^*,P_{in})} := \frac{\frac{|T_i|}{16}\left|\sum_{l=1}^{16}\phi_k(c_{i,l})\cdot\left\{V^h_{T_i}(c_{i,l})+\Delta t\sum_{j=1}^{2}A^{0^{-1}}(U_{ci})A_j(u_{ci})A^0(U_{ci})\,\partial_{x_j}V\big|_{T_i}\right\}\right|}{\sqrt{\frac{|T_i|}{16}\sum_{l=1}^{16}\left\{\left(\phi_k(c_{i,l})\right)^2+\Delta t\left(\sum_{j=1}^{2}A^{0^{-1}}(U_{ci})A_j(u_{ci})A^0(U_{ci})\partial_{x_j}\phi_k(c_{i,l})\right)^2\right\}}}$$

(6.3)
as an approximation to the dual graph norm error indicator.

The adaptive procedure using this refinement indicator is as follows. Given two tolerances $\mathrm{TOL}_{\mathrm{refine}}$ and $\mathrm{TOL}_{\mathrm{coarse}}$ the adaptive algorithm sweeps through the grid at certain times and refines all those triangles, for which

$$\|r^h\|_{\Delta'(\mathscr{L}^*,P_{in})} < \mathrm{TOL}_{\mathrm{refine}}$$

is valid, while triangles are deleted from the mesh for which

$$\|r^h\|_{\Delta'(\mathscr{L}^*,P_{in})} > \mathrm{TOL}_{\mathrm{coarse}},$$

holds.

7 Numerical experiments

To show the ability of our refinement indicator in resolving flow phenomena we apply the DLR-τ-Code together with the approximated error indicator (6.3) to several test problems. In all cases the approximate Riemann solver of Roe was used as the numerical flux function together with the usual entropy fix to exclude stable expansion shocks.

7.1 Transonic steady flow about NACA0012

The first test problem is transonic steady flow about a NACA0012 airfoil in which the onflow conditions are given by

$$\mathrm{Ma}_\infty = 0.8, \quad \alpha = 1.25^\circ$$

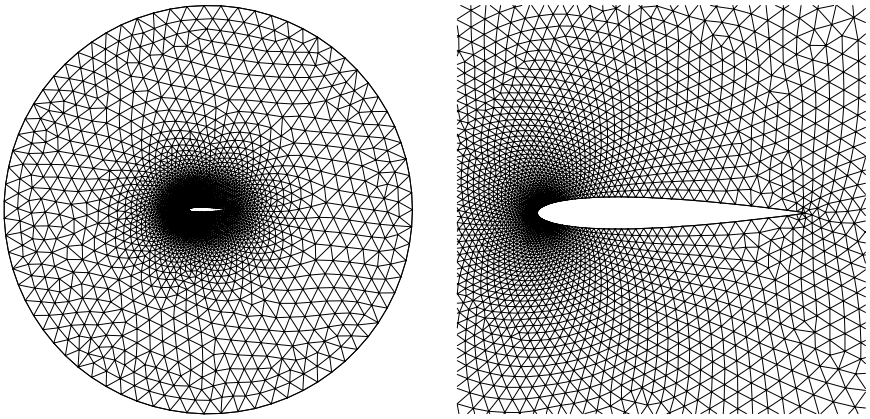

Fig. 9. Initial grid for transonic flow about NACA0012 airfoil

where α denotes the angle of attack. Note that we non-dimensionalised the Euler equations with the onflow velocity and not with the speed of sound.
The dominant flow features in this particular case are a strong shock on the upper side of the airfoil and a weak one on its lower side. It was shown in [21] that classical refinement indicators based on gradients of flow variables often have problems in detecting the weak shock if the initial grid is not fine enough. Thus, as a first test, the new refinement indicator should detect the weak lower side shock. The initial grid used is the one shown in Fig. 9 and is the same that was used in [21]. The density distribution on this grid can be seen in Fig. 10. If the refinement indicator (6.2) is used after 1000 timesteps the resulting grid after 3 adaption periods is shown in Fig. 11. The refinement indicator has detected both, the strong shock on the upper side of the airfoil and the weak shock on the lower side. Parts of the supersonic bubble on the upper side are also adapted but the size of the adapted region depends more strongly on the size of the user-given tolerance.

The corresponding density distribution is shown in Fig. 12. The same number of isolines (i.e. not the same values of density) was used in the presentation of the adapted as well as in the figure showing the non-adapted solution.

7.2 Supersonic steady flow about a cylinder

The next problem we consider is the supersonic flow about a cylinder where the onflow Mach number is given by

$$\mathrm{Ma}_\infty = 3.0.$$

We start with an initial grid as shown in Fig. 13. The distance between the cylinder of radius $r = 2$ and the bow shock should be $d = 1.703$ as can be estimated from linearised theories, compare [26]. The solution of the DLR-τ-Code is shown in the right half of Fig. 13 where the density distribution can be seen. Applying

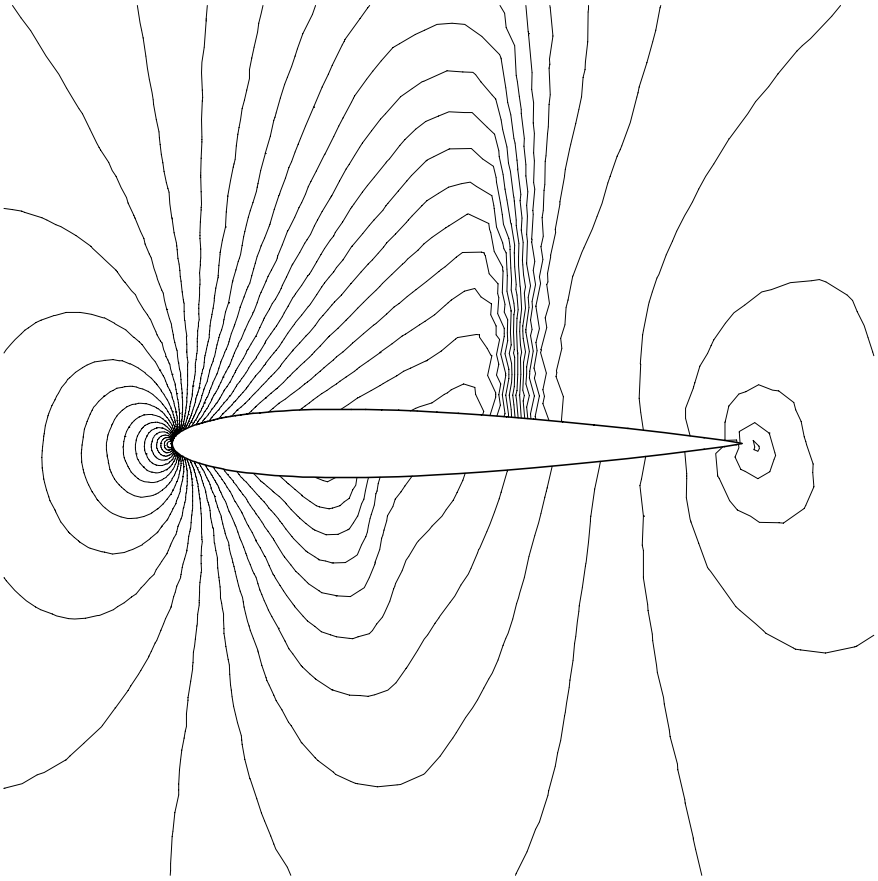

Fig. 10. Density distribution on the initial grid

the adaptive techniques of the DLR-τ-code triggered by our refinement indicator (6.3) gives the grid and numerical solution as shown in Fig. 14. Besides the bow shock, which is captured at the correct position, the grid is also refined at the outflow boundaries down to the body surface. The solution around the stagnation point suffers from the carbuncle phenomenon of Roe's approximate Riemann solver which is only slightly surpressed by our choice of the entropy fix.

7.3 Supersonic unsteady flow in a channel

Some years ago Woodward and Colella proposed a model problem that is now accepted as one of the standard test cases for numerical methods for unsteady Euler equations, see [25]. A supersonic flow is established in a channel and at time $t = 0$ a forward facing step on the lower side of the channel is suddenly introduced. The onflow Mach number in this problem is

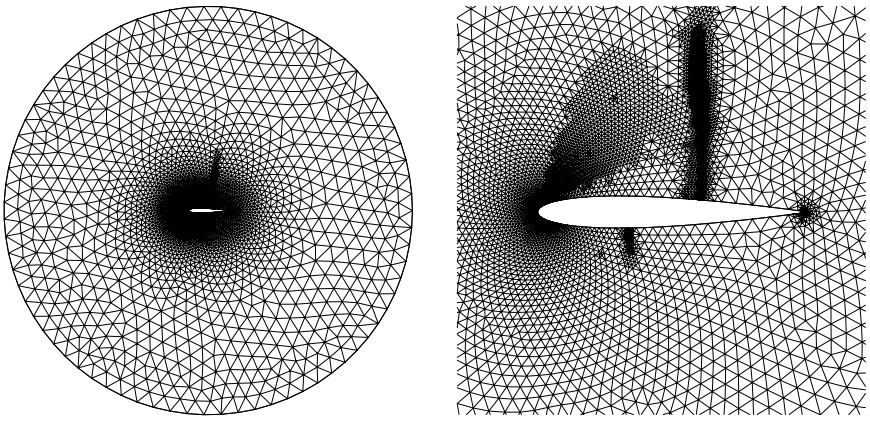

Fig. 11. Grid after three adaption cycles for transonic flow about NACA0012 airfoil

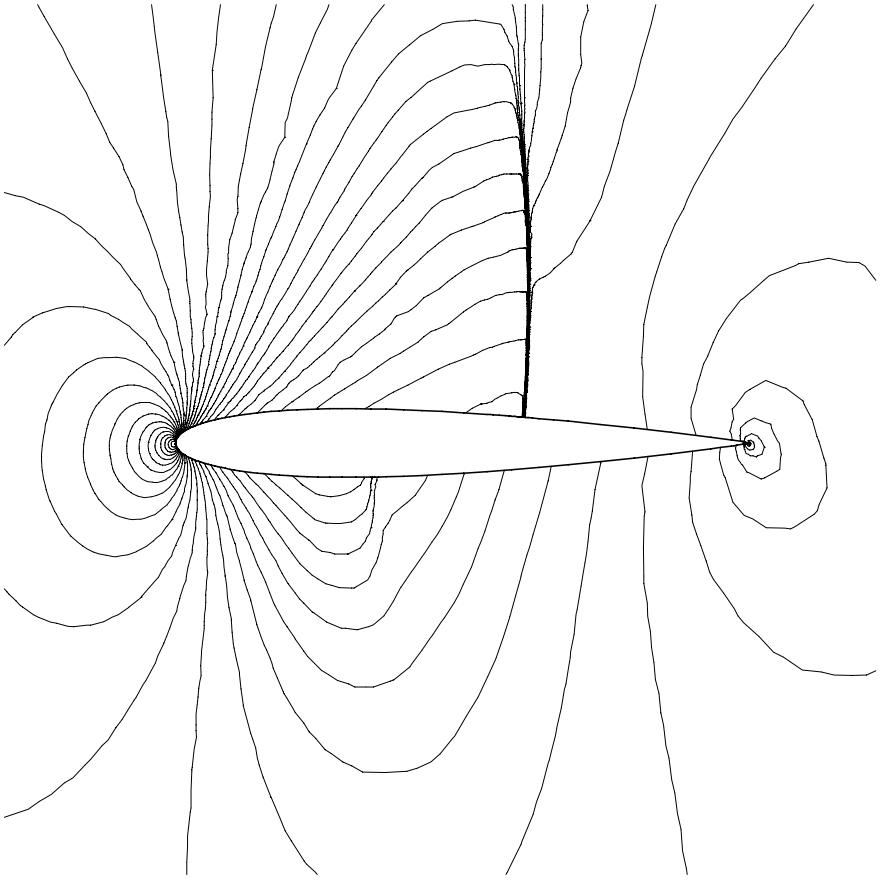

Fig. 12. Density distribution on the adapted grid

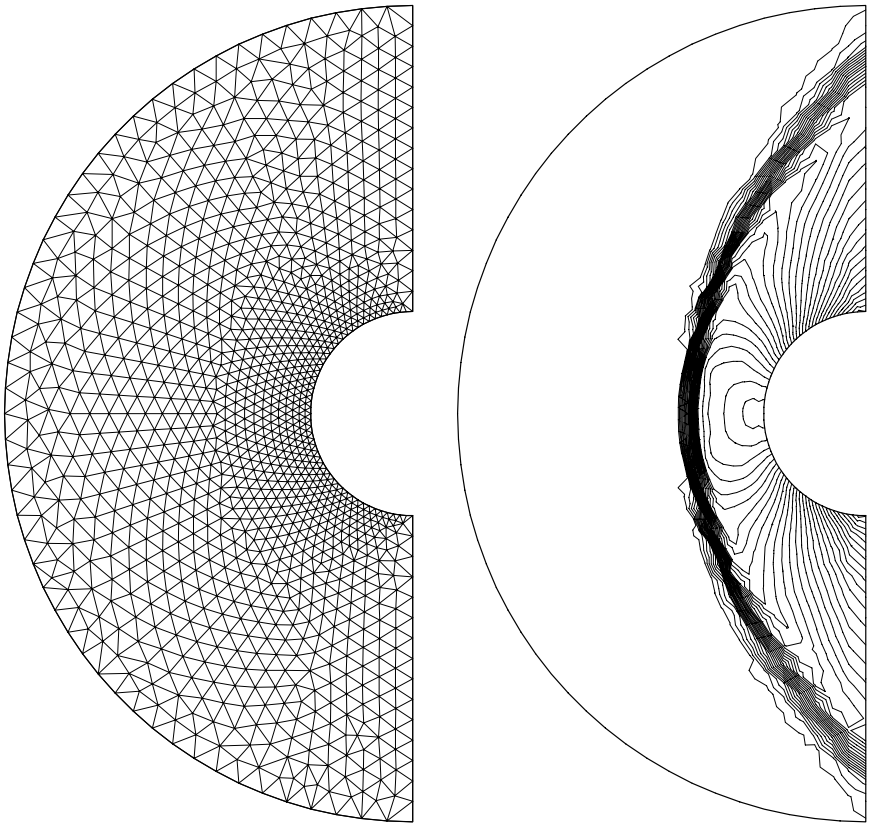

Fig. 13. Initial grid and density distribution

$$\mathrm{Ma}_\infty = 3.0$$

while the flow is parallel to the channel walls. The most interesting flow phenomena are present in the flow at time $t = 8$ when a shock system is fully developed within the channel. Note that Woodward and Colella used the onflow speed of sound to non-dimensionalise the Euler equations so that our time $t = 8$ corresponds to their time $t = 4$.

Figure 15 shows the grid at time $t = 0.119$. The bow shock has just detached from the step and starts moving around the corner.

A detail of the grid and the corresponding density distribution can be seen in Fig. 16. The grid at time $t = 0.67$ and the corresonding density are shown in Fig. 17. At time $t = 1.44$ the bow shock is already attached to the upper wall of the channel. As can be seen from Fig. 18 the refinement of the grid follows the development of the flow phenomena accurately. A reflected shock is now moving downstream. Figure 19 shows grid and density distribution at time $t = 2.48$. The first reflected shock is just touching the lower wall.

Approximately at time $t = 4$ the overall shock structure is established in the channel. From that time on the dynamics of the flow field change drastically and

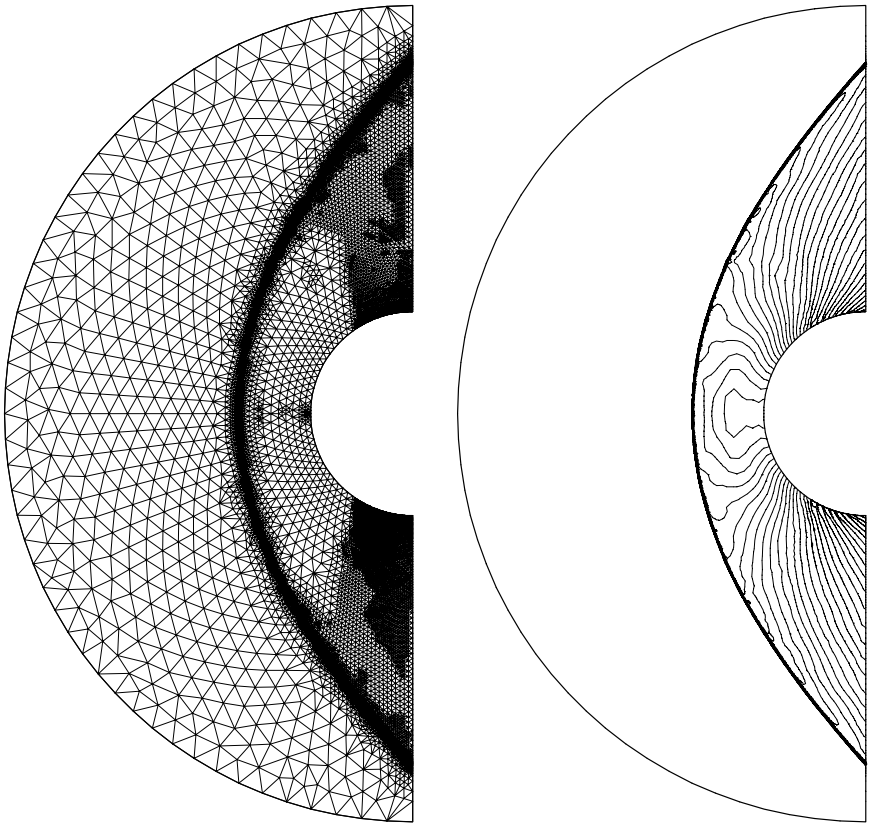

Fig. 14. Adapted grid and density distribution

start to influence the refinement indicator. Before $t = 4$ a drastic temporal change of the flow field can be observed in the sense that flow phenomena, like shocks, move with high relative velocity. After $t = 4$ temporal changes are negligible and all structures of the flow field move very slowly and do not change very much between $t = 4$ and $t = 8$. As a consequence, the detected error exceeds the user-given tolerances $\mathrm{TOL}_{\mathrm{refine}}$ and $\mathrm{TOL}_{\mathrm{coarse}}$. To take this behaviour of the flow field into account we had to change the refinement tolerance bounds within the computation. The adaptive tuning of the tolerance bounds makes sense since our refinement indicator is a space-time indicator. Thus, temporal as well as spatial errors contribute to the overall error.

Figure 20 shows the grid and the density distribution at time $t = 4.77$. As can be seen the structural details of the solution are already fully developed. Note that the second reflected shock is already poorly treated by the adaption process. Changing the refinement limits we get the final solution and grid at time $t = 8$ shown in Fig. 21. In contrast with the ad hoc refinement indicators presented in [21] and [22] the dual graph norm refinement indicator triggered the adaptive algorithm to refine the greater vicinity of the contact discontinuity.

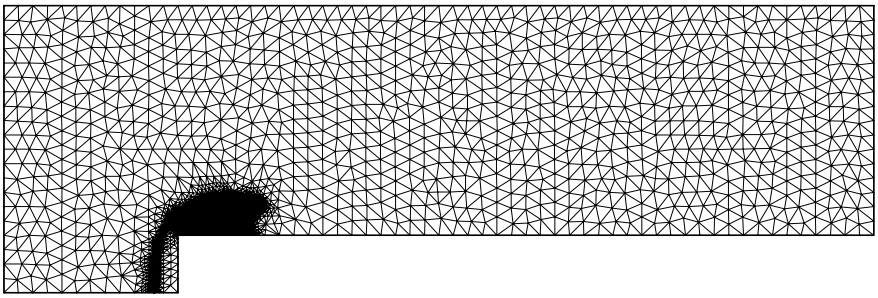

Fig. 15. Adapted grid and detail of the grid at $t = 0.119$

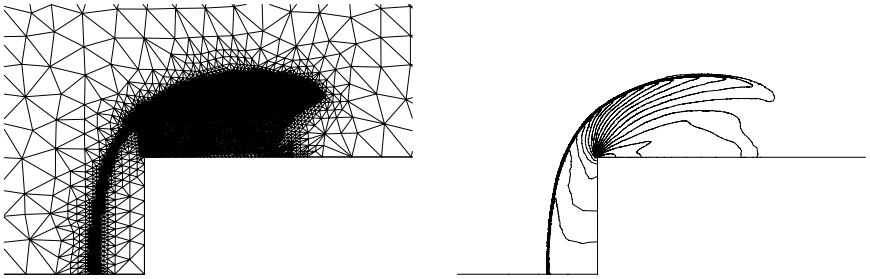

Fig. 16. Detail of the adapted grid and density distribution at $t = 0.119$

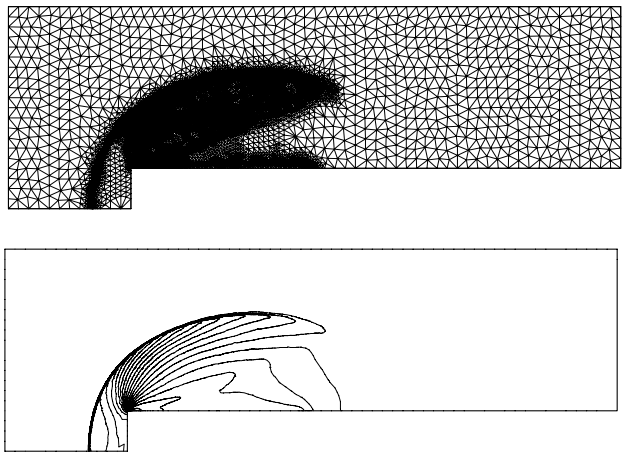

Fig. 17. Adapted grid and density distribution at $t = 0.67$

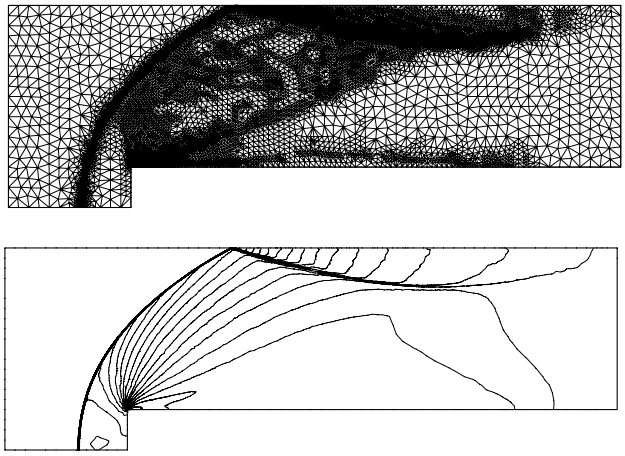

Fig. 18. Adapted grid and density distribution at $t = 1.44$

Figure 22 shows the Mach number distribution on the final grid. The results compare well with results obtained with other residual based error indicators but in contrast with them, the dual graph norm indicator is a true rather than ad hoc error indicator.

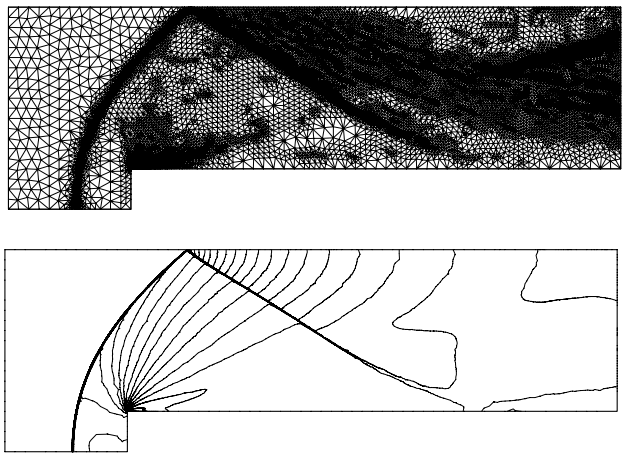

Fig. 19. Adapted grid and density distribution at $t = 2.48$

8 Conclusions

We have presented a new refinement indicator applicable to adaptive computations of solutions of symmetric hyperbolic systems. A two-sided error bound on the dual graph norm of the residual of the numerical approximation is proved and thus this dual graph norm refinement indicator is a true error indicator. The

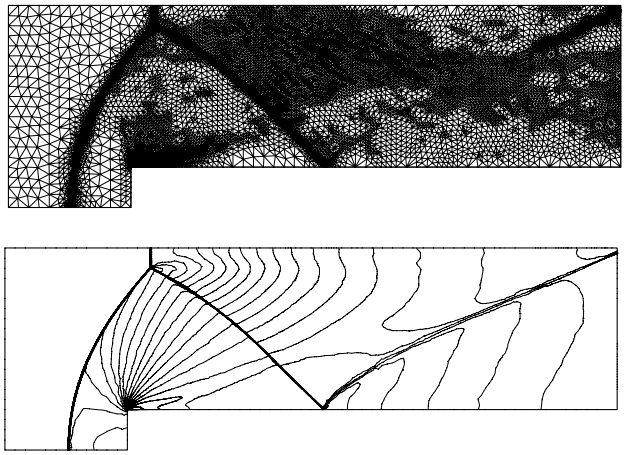

Fig. 20. Adapted grid and density distribution at $t = 4.77$

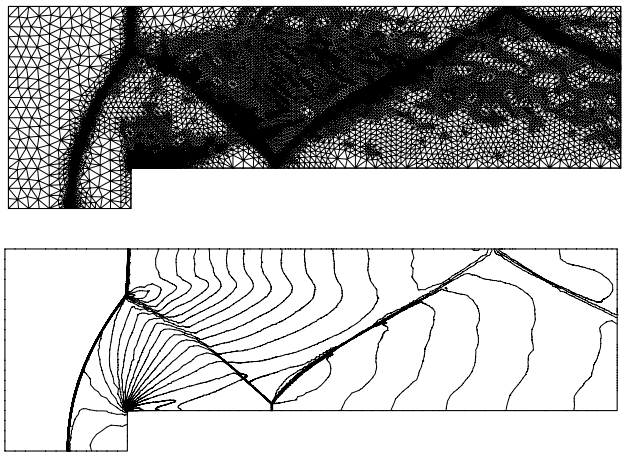

Fig. 21. Adapted grid and density distribution at $t = 8$

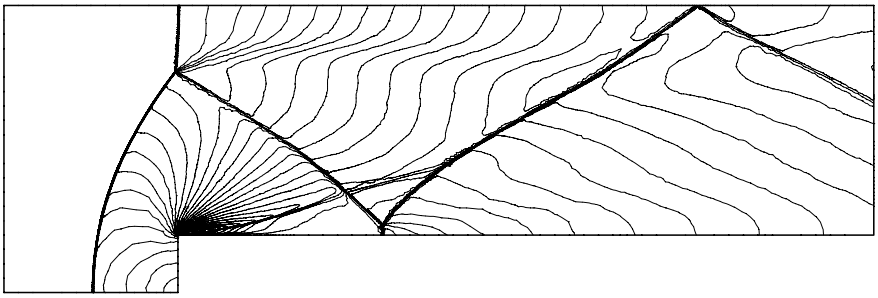

Fig. 22. Mach number distribution at $t = 8$

Euler equations of gas dynamics are symmetrised by means of entropy variables and locally linearised about a mean constant state. In this form the dual graph norm refinement indicator is applicable in adaptive algorithms for inviscid compressible flow problems. We developed a careful discrete approximation to the dual graph norm indicator in the framework of the DLR-τ-Code and applied the new refinement indicator to steady as well as unsteady test problems. For further analytical results on the dual graph norm and its relationship with $h\|r^h\|_{L^2(P_{in})}$ we refer to [24].

Acknowledgements. The authors would like to thank Oliver Friedrich and Daniel Hempel, then at the Institute for Fluid Mechanics, DLR Göttingen, for providing a parallel version of the τ-Code. The case of the supersonic flow in a channel with a forward facing step was computed on an IBM SP1 computer with 8 nodes using their code.

The authors gratefully acknowledge the fruitful collaborative work with their colleagues J. Mackenzie (University of Strathclyde, Glasgow) and G. Warnecke (Otto-von-Guericke-Universität, Magdeburg).

The work reported here was carried out as part of the collaborative research project funded by DAAD and the British Council through the ARC-programme 313-ARC-VII-93. The authors gratefully acknowledge DAAD and the British Council for the financial support of this exchange programme.

References

1. Bank, R.E., Sherman, A.H., Weiser, A. (1983): Refinement Algorithms and Data Structures for Regular Local Mesh Refinements. in: Scientific Computing; Stepleman, R. et. al. (eds.), Amsterdam: IMACS North-Holland, pp. 3–17.
2. Ciarlet, P.G. (1978): The Finite Element Method for Elliptic Problems. North-Holland.
3. Feistauer, M. (1993): Mathematical Methods in Fluid Dynamics. Longman Scientific & Technical, Harlow.
4. Fezoui, L., Stoufflet, B. (1989): A Class of Implicit Upwind Schemes for Euler Simulations with Unstructured Meshes. J. Comp. Phys. **84**, pp. 174–206.
5. Friedrichs, K.O. (1958): Symmetric Positive Linear Differential Operators. Comm. Pure Appl. Math. **11**, pp. 333–418.
6. Geiben, M., Kröner, D., Rokyta, M. (1993): A Lax-Wendroff Type Theorem for Cell-Centered, Finite Volume Schemes in 2-D. Report No.278, Sonderforschungsbereich 256, Rheinische Friedrich-Wilhelms-Universität, Bonn.
7. Hansbo, P., Johnson, C. (1991): Adaptive Streamline Diffusion Methods for Compressible Flow Using Conservation Variables. Comp. Meth. Appl. Mech. and Eng. **87**, pp. 267–280.
8. Harten, A., Lax, P.D. (1981): A Random Choice Finite Difference Scheme for Hyperbolic Conservation Laws. SIAM J. Num. Anal. **18**, pp. 289–315.
9. Hempel, D. (1993): Local Mesh Adaption in Two Space Dimensions. Impact of Comp. in Sci. and Eng. **5**, pp. 309–317.
10. Hempel, D.: Isotropic Red-Green Adaption. In preparation.
11. Lax, P.D., Phillips, R.S. (1960): Local Boundary Conditions for Dissipative Symmetric Linear Differential Operators. Comm. Pure Appl. Math. **13**, pp. 427–455.
12. Heinrich, B. (1987): Finite Difference Methods on Irregular Networks. Birkhäuser Verlag, ISNM Vol.82.
13. Hughes, T.J.R., Franca, L.P., Mallet, M. (1986): A New Finite Element Formulation for Computational Fluid Dynamics: I. Symmetric Forms of the Compressible Euler and Navier-Stokes Equations and the Second Law of Thermodynamics. Comp. Meth. Appl. Mech. Eng. **54**, pp. 223–234.
14. Kornhuber, R., Roitzsch, R. (1989): On Adaptive Grid Refinement in the Presence of Internal or Boundary Layers. Preprint SC 89-5, Konrad-Zuse-Zentrum Berlin.

15. Mackenzie, J.A., Süli, E., Warnecke, G. (1994): A Posteriori Analysis for Petrov-Galerkin Approximations of Friedrichs Systems. Manuscript.
16. Mackenzie, J.A., Süli, E., Warnecke, G. (1994): A Posteriori Error Estimates for the Cell-Vertex Finite Volume Method. in: Adaptive Methods: Algorithms, Theory and Applications. Hackbusch, W., Wittum, G. (eds.), Vieweg, Braunschweig, pp. 221–235.
17. Meister, A. (1994): Ein Beitrag zum DLR-τ-Code: Ein explizites und implizites Finite-Volumen-Verfahren zur Berechnung instationärer Strömungen auf unstrukturierten Gittern. DLR Internal Report, IB 223-94 A 36, Institute for Fluid Mechanics, DLR Göttingen.
18. Mock, M.S. (1980): Systems of Conservation Laws of Mixed Type. J. Diff. Equ. **37**, pp. 70–88.
19. Sonar, Th. (1995): Multivariate Rekonstruktionsverfahren zur numerischen Berechnung hyperbolischer Erhaltungsgleichungen. Habilitationsschrift, TH Darmstadt.
20. Sonar, Th. (1993): On the Design of an Upwind Scheme for Compressible Flow on General Triangulations. Numerical Algorithms **4**, pp. 135–149.
21. Sonar, T. (1993): Strong and Weak Norm Refinement Indicators Based on the Finite Element Residual for Compressible Flow Computation. IMPACT of Comp. in Sci. and Eng. **5**, pp. 111–127.
22. Sonar, T., Hannemann, V., Hempel, D. (1994): Dynamic Adaptivity and Residual Control in Unsteady Compressible Flow Computation. Mathematical and Computer Modelling **20**, pp. 201–213.
23. Steger, J.L., Warming, R.F. (1980): Flux Vector Splitting of the Inviscid Gas Dynamic Equations with Applications to Finite Difference Methods. J. Comp. Phys. **40**, pp. 263–293.
24. Süli, E. (1995): A posteriori error analysis and global error control for adaptive finite element approximations of hyperbolioc problems. Oxford University Computing Laboratory Technical Report 95/14. To appear in: Griffiths, D.F. (ed.), Proceedings of the 16th International COnference on Numerical Analysis, Dundee, June 1995, Longmans.
25. Woodward, P., Colella, P. (1984): The Numerical Simulation of Two-Dimensional Fluid Flow with Strong Shocks. J. Comp. Phys. **54**, pp. 115–173.
26. Zierep, J. (1976): Theoretische Gasdynamik. Verlag G. Braun, Karlsruhe.

This article was processed by the author using the LaTeX style file *pljour1m* from Springer-Verlag.